A hybrid stochastic Galerkin method for uncertainty quantification applied to a conservation law modelling a clarifier-thickener unit with several random sources

Andrea Barth · Raimund Bürger · Ilja Kröker · Christian Rohde

Abstract The continuous sedimentation process in a clarifier-thickener can be described by a scalar nonlinear conservation law for the local solids volume fraction whose flux density function is discontinuous with respect to spatial position due to feed and discharge mechanisms. In the applications of this model, which include mineral processing and wastwater treatment, the rate and composition of the feed flow cannot be given deterministically. Efficient numerical simulation is required to quantify the effect of uncertainty in these control parameters in terms of the response of the clarifier-thickener system. Thus, the problem at hand is one of uncertainty quantification for nonlinear hyperbolic problems with several random perturbations. To solve it, a hybrid stochastic Galerkin (HSG) method is devised that extends the classical polynomial chaos approximation by multiresolution discretization in the stochastic space. The approach leads to a deterministic hyperbolic system for a finite number of stochastic moments which is however partially decoupled and thus allows efficient parallelisation. The complexity of the problem is further reduced by stochastic adaptivity. For the approximate solution of the resulting high-dimensional system a finite volume scheme is introduced. Several numerical experiments are presented.

Keywords clarifier-thickener model · polynomial chaos · uncertainty quantification · Galerkin projection · hybrid stochastic Galerkin · finite volume method

A. B., I. K. and C. R. would like to thank the German Research Foundation (DFG) for financial support of the project within the Cluster of Excellence in Simulation Technology (EXC 310/1) at the University of Stuttgart. R. B. is supported by Fondecyt project 1130154; Conicyt project Anillo ACT1118 (ANANUM); Red Doctoral REDOC.CTA, MINEDUC project UCO1202 at Universidad de Concepción; BASAL project CMM, Universidad de Chile and Centro de Investigación en Ingeniería Matemática (CI^{2}MA), Universidad de Concepción; and Centro CRHIAM Proyecto Conicyt Fondap 15130015.

Andrea Barth
IANS, Universität Stuttgart, Pfaffenwaldring 57, D-70569 Stuttgart, Germany, E-mail: barthaa@mathematik.uni-stuttgart.de

Raimund Bürger
CI^{2}MA and Departamento de Ingeniería Matemática, Universidad de Concepción, Casilla 160-C, Concepcion, Chile, E-mail: rburger@ing-mat.udec.cl

Ilja Kröker · Christian Rohde
IANS, Universität Stuttgart, Pfaffenwaldring 57, D-70569 Stuttgart, Germany, E-mail: ikroeker|crohde@mathematik.uni-stuttgart.de

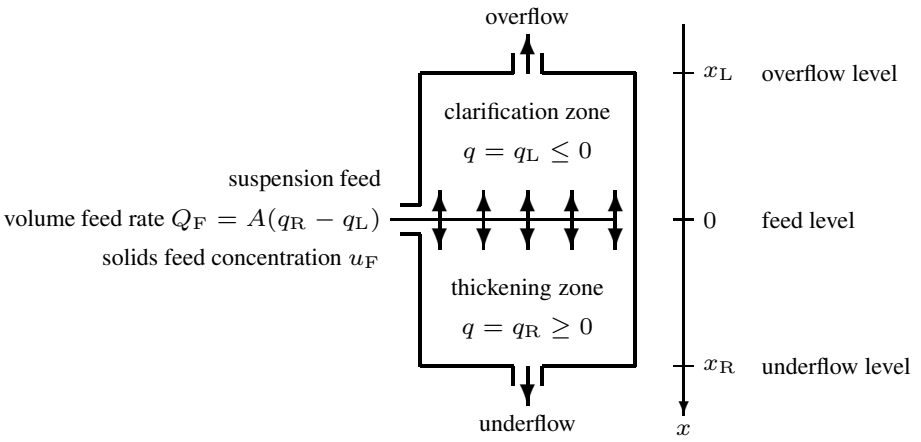

Fig. 1 Principle of the clarifier-thickener (CT) model. The cylindrical unit of cross-sectional area A is assumed to occupy the depth interval $[x_{\mathrm{L}}, x_{\mathrm{R}}]$. Suspension to be separated is fed at level $x = 0$ at rate Q_{F} and concentration u_{F}. The feed flow is split into upwards- and downwards-directed bulk flows with respective velocities $q_{\mathrm{L}} \leq 0$ and $q_{\mathrm{R}} \geq 0$. Note that in the deterministic setting, u_{F}, Q_{F} and q_{R}, and therefore also q_{L}, are known control parameters. Under normal circumstances, concentrated sediment forms on the bottom of the thickening zone and is continuosly removed with the underflow while clarified liquid laves the unit with the overflow. It is assumed that the solid-liquid separation takes place within the unit only, identified by the x-interval $(x_{\mathrm{L}}, x_{\mathrm{R}})$, while outside, in the overflow and underflow streams, both phases move at the same velocity.

1 Introduction

1.1 Scope

Modelling uncertainty is important in many technical applications in which one seeks to quantify the stochastic variability of the response of a nonlinear system, usually defined by the solution of a time-dependent partial differential equation (PDE), with respect to uncertainty in input data such as initial conditions, control parameters and PDE coefficient functions. Straightforward Monte Carlo (MC) sampling of solutions produced under stochastic variation of the input data is easily implemented, but quantifying randomness via MC sampling is computationally very inefficient due to the slow convergence of stochastics. The quantification of randomness by stochastic Galerkin (SG) or collocation methods leads to deterministic models for at least a finite number of stochastic moments (cf. [30] for an overview), and seems to be a more promising technique in the present situation. While this approach is supported by a meanwhile well-understood theory for models posed in terms of linear PDEs, for nonlinear problems first steps have been done just recently [**?**,32,34,35]. One important subclass of nonlinear problems are hyperbolic conservation laws, on which the present work is focused.

It is the purpose of this paper to extend the hybrid stochastic Galerkin (HSG) discretization introduced in [9,25,26] to several stochastic dimensions, and to apply it to an applicative model governed by a scalar, nonlinear hyperbolic conservation law. Specifically, we consider a clarifier-thickener (CT) model for the continuous solid-liquid separation of suspensions under gravity [5,16,18–21], see Figure 1. This model is a strongly idealized description of secondary settling tanks in wastewater treatment or of thickeners in mineral pro-

cessing [7]. For so-called ideal suspensions of small solid, non-flocculent particles that do not exhibit the effect of sediment compressibility, the governing PDE is a first-order scalar conservation law with a flux density function that depends spatially on position, along with suitable initial conditions and control variables. The well-posedness and numerical analysis of this equation forms a research topic in itself [5,7,16,18–21], since the entropy solution concept for this model does not emerge as a straightforward limit case of the theory a conservation law with smoothly varying coefficients [27], at least unless one imposes further conditions on the relative sizes of the flux smoothing and the parabolic regularization of the vanishing viscosity method (cf., e.g., [8,15,17]).

In the clarifier-thickener related multiphase flow models, many input parameters cannot be described with deterministic accuracy but behave stochastically. For instance, in mineral processing the uncertainty comes from the fact that the feed flow stems from other units that are not under control of the CT operator, while in wastewater treatment weather conditions, which may affect the operation of the unit, are unpredictable. In [9] we analyzed the effect of uncertainty in one scalar quantity, namely the feed concentration u_{F}. This uncertainty produces a first-order scalar conservation law with a random flux function. In this work we provide a new efficient method for evaluating the uncertainty of the response of the system, that is, of the exact or numerical solution of the governing PDE, in terms of the uncertainty in *three* control parameters, namely u_{F} and the so-called bulk flows, denoted by q_{L} and q_{R}. (Uncertainty in q_{L} and q_{R} can equivalently be expressed as uncertainty in the volume feed flow, equivalent to $q_{\mathrm{R}} - q_{\mathrm{L}}$, and at the same time in CT control actions, which are expressed by q_{R}.)

As a by now classical approach in uncertainty quantification one could apply the SG method where the random field is represented in terms of orthonormal polynomials. This leads to a very accurate approximation in form of a strongly coupled, high-dimensional deterministic system for a finite number of moments [32]. On the other hand, one might apply the multi-wavelet stochastic discretization as e.g. in [35]. This approach still leads to a full coupling of the polynomial basis, which is defined on the whole stochastic domain. In contrast to this, the approach advanced in the present paper consists in the application of a hybrid stochastic Galerkin (HSG) method that combines polynomial chaos (PC) and multi-wavelet representations, such that each stochastic element is equipped with its own polynomial basis. This combination has the decisive advantage that the HSG method leads to a partially decoupled deterministic system that allows efficient parallelization. Furthermore, we improve the efficiency of the HSG method by an adaptive multiresolution concept in the stochastic space (see also [9,29] for an adaptive approach in the framework of multiresolution techniques).

1.2 Outline of the paper

The remainder of the paper is organized as follows. In Section 2 the governing model is described. To this end we summarize in Section 2.1 a deterministic, spatially one-dimensional CT model corresponding to Figure 1. In Section 2.2 we state the final form of the one-dimensional model that also includes the random perturbations in two and three random variables. In Section 3 we introduce an approximation for the random perturbations by the SG and the new HSG approaches. Specifically, we review the PC approach in Section 3.1 and define in Section 3.3 the SG system. This leads after a finite volume discretization in the one-dimensional physical space to the stochastic Galerkin finite volume (SG-FV) method. In Section 3.4 we extend the SG stochastic discretisation to the hybrid stochastic Galerkin

(HSG) approach. In Section 3.4.1 we explain how the coefficients of the HSG representation are calculated. Next, in Section 3.4.2 we discuss the extension of HSG to several stochastic dimensions and consider their application to the clarifier-thickener model in Section 3.4.3. A fully discrete finite volume formulation for the SG approaches, namely the respective "HSG–system" is introduced in Section 3.4.4 (HSG-FV). The further improvement of the method is stochastic adaptivity (denoted as HSG–adapt), which is introduced in Section 4. The HSG-adapt method reduces the stochastic dimension and increases the computational efficiency decisively. Section 4 starts with a short description of properties of the multi-wavelet basis in Section 4.1 and proceeds with the extension to the multivariate case in Section 4.2. In Section 4.3 we recapitulate the concept of the graded tree and introduce a N_{r}-adaptivity algorithm for the HSG-discretization based on this concept. Section 5 is devoted to the presentation of numerical examples. In Section 5.1 we consider the application of the FV methods introduced in Section 3.4.4. We present experiments in two and three stochastic dimensions and compare the HSG-FV results with those of the Monte Carlo approach. In Section 5.2 we discuss the benefits of the parallel application for HSG methods. The numerical experiments in Section 5.3 confirm the efficiency and accuracy of the HSG-adapt method. In Section 6 we present the application of the HSG approach on the real world problem. Conclusions of the paper are summarized in Section 7.

2 Governing models

2.1 Deterministic version

Here we briefly summarize the one-dimensional clarifier-thickener (CT) model (Figure 1); see, e.g., [5] for a detailed derivation. The model is based on the conservation equations of the solid and the fluid. Both are considered as superimposed continuous phases with velocities v_{s} and v_{f}, respectively. In terms of the solid-fluid relative velocity $v_{\mathrm{r}} := v_{\mathrm{s}} - v_{\mathrm{f}}$ and the volume-average velocity of the mixture $q := uv_{\mathrm{s}} + (1-u)v_{\mathrm{f}}$, where $u = u(x,t)$ is the local solids volume fraction, the continuity equations can be written as follows:

$$u_t + \big(uq + u(1-u)v_{\mathrm{r}}\big)_x = 0, \quad q_x = 0, \quad x \in D \subset \mathbb{R}, \quad t > 0. \tag{1}$$

Here the first equation represents the conservation of mass of solids and the second that of the mixture. Following the well-known kinematic theory of sedimentation [5,28], we introduce the constitutive assumption that v_{r} is a given function of u; specifically, we write

$$v_{\mathrm{r}} = v_{\mathrm{r}}(u) = \frac{b(u)}{u(1-u)},$$

where $b = b(u)$ is the so-called Kynch batch flux density function [28]. A common functional form of $b(u)$ is given by the Richardson-Zaki expression [33]:

$$b^{\mathrm{RZ}}(u) := \begin{cases} u_\infty u(1-u)^{n_{\mathrm{RZ}}} & \text{for } 0 \le u \le u_{\max}, \\ 0 & \text{for } u < 0 \text{ and } u > u_{\max}, \end{cases}$$

where $u_\infty > 0$ is the Stokes velocity, that is, the settling velocity of a single particle in an unbounded domain, $0 < u_{\max} \le 1$ is a maximal solids concentration, and $n_{\mathrm{RZ}} \ge 1$ is a

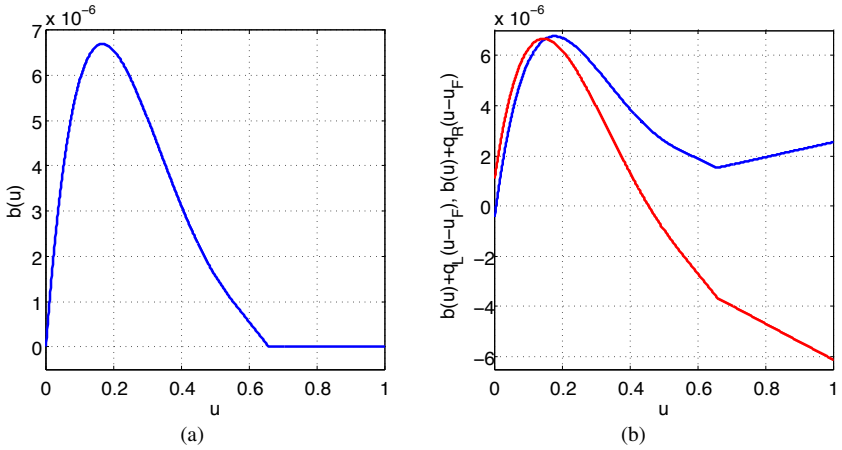

Fig. 2 (a) Batch flux density function $b(u)$ given by (2) with $u_\infty = 10^{-4}\,\mathrm{m/s}$, $n_{\mathrm{RZ}} = 5$ and $u_* = 0.55$, (b) Fluxes $b(u) + q_{\mathrm{R}}(u - u_{\mathrm{F}})$ in the thickening zone (blue) and $b(u) + q_{\mathrm{L}}(u - u_{\mathrm{F}})$ in the sedimentation zone (red).

parameter. However, we herein define $b(u)$ by the following modified form of $b^{\mathrm{RZ}}(u)$:

$$b(u) = \begin{cases} u_\infty u(1-u)^{n_{\mathrm{RZ}}} & \text{for } 0 \le u \le u_*, \\ p_2(u) & \text{for } u_* < u \le u_{\max} := u_* - b^{\mathrm{RZ}}(u_*)/b^{\mathrm{RZ}\prime}(u_*), \\ 0 & \text{for } u > u_{\max}, \end{cases} \tag{2}$$

where $p_2(u) = \alpha u^2 + \beta u + \gamma$ is the unique second-order polynomial satisfying $p_2(u_*) = b^{\mathrm{RZ}}(u_*)$, $p_2'(u_*) = b^{\mathrm{RZ}\prime}(u_*)$ and $p_2(u_{\max}) = 0$. The insertion of p_2 between u_* and $u_{\max}$ ensures that b is Lipschitz continuous with support on $[0, u_{\max}]$, continuously differentiable on $(0, u_{\max})$, and its left-sided derivative at $u_{\max}$ is negative.

Realistic parameter values are $u_\infty = 10^{-4}\,\mathrm{m/s}$ and $n_{\mathrm{RZ}} = 5$. If we choose, moreover, $u_* = 0.55$, then $u_{\max} = 0.657608695652174$, which is close to the maximum packing density of equal-sized spheres. Figure 2(a) shows the resulting function $b(u)$. This function will be employed in the numerical experiments.

For a cylindrical vessel without sources and sinks, the equation $q_x = 0$ in (1) means that q is a constant with respect to x. For a continuously operated CT unit (see Figure 1), we assume that the unit occupies the depth interval $x \in [x_{\mathrm{L}}, x_{\mathrm{R}}]$, where x_{L}, $x = 0$ and x_{R} are the overflow, feed, and underflow levels, respectively. Moreover, the bulk velocity $q = q(x,t)$ (velocity of the mixture) is given by

$$q(x,t) = \begin{cases} q_{\mathrm{L}}(t) & \text{for } x < 0, \\ q_{\mathrm{R}}(t) & \text{for } x > 0, \end{cases}$$

where it is understood that $q_{\mathrm{L}}(x,t) \le 0$ and $q_{\mathrm{R}}(x,t) \ge 0$, and global conservation is ensured by

$$Q_{\mathrm{F}}(t) = (q_{\mathrm{R}} - q_{\mathrm{L}})A. \tag{3}$$

Under the present assumptions we may rewrite the first equation in (1) as a conservation law $u_t + h(x,t,u)_x = 0$ with the nonlinear flux

$$h(x,t,u) = \gamma^1(x,t)u(x,t) + \gamma^2(x)b(u),$$

where we define the discontinuous (with respect to x) parameters

$$\gamma^1(x,t) := \begin{cases} q_{\mathrm{L}}(t) & \text{for } x < 0, \\ q_{\mathrm{R}}(t) & \text{for } x > 0, \end{cases} \qquad \gamma^2(x) := \begin{cases} 1 & \text{for } x \in (x_{\mathrm{L}}, x_{\mathrm{R}}), \\ 0 & \text{for } x \notin (x_{\mathrm{L}}, x_{\mathrm{R}}). \end{cases}$$

Finally, representing the solids feed mechanism by a singular source term involving the Dirac δ-symbol, we arrive at the following governing equation for $D_T := \mathbb{R} \times (0,T)$:

$$u_t(x,t) + \big(h(x,t,u(x,t))\big)_x = \delta(x)\frac{Q_{\mathrm{F}}(t)u_{\mathrm{F}}(t)}{A} \quad \text{on } D_T, \tag{4}$$

which is solved along with the initial condition

$$u(x,0) = u_0(x) \quad \text{for } x \in \mathbb{R}.$$

The uncertainty in u_{F}, q_{L} and q_{R} will be introduced in Section 2.2. If uncertainty is not built in, then the presented model is equivalent to the one-dimensional clarifier-thickener models studied in [5,6].

2.2 Random perturbation and final formulation of models

In this work we assume that the feed concentration u_{F} exhibits stochastic variability and that also the upward- and downward-directed bulk flows q_{L} and q_{R} are subject to random perturbations. (In light of (3) this is equivalent to assume stochastic variability of Q_{F} and of one of the variables q_{L} and q_{R}.) In fact, for the probability measure $\mathcal{P}$ let $(\Omega, \mathcal{P}, \mathcal{F})$ be the probability space. We denote the random feed volume fraction by $u_{\mathrm{F}} = u_{\mathrm{F}}(\omega_1) \in [0,1]$, where $\omega_1 \in \Omega$. The random perturbed upward- and downward-directed bulk flows are denoted by $q_{\mathrm{L}}(\omega_2)$ and $q_{\mathrm{R}}(\omega_3)$, where $\omega_2, \omega_3 \in \Omega$. The complete feed term in (4) can be rewritten as part of the flux such that (4) becomes a nonlinear conservation law with discontinuous flux. For this purpose we rewrite the source term as a part of the convective flux via

$$\delta(x)Q_{\mathrm{F}}(t,\omega_2,\omega_3)u_{\mathrm{F}}(t,\omega_1) = \big(H(x)Q_{\mathrm{F}}(t,\omega_2,\omega_3)u_{\mathrm{F}}(t,\omega_1)\big)_x,$$

where H denotes the Heaviside function. Thus, defining the vector $\boldsymbol{\omega} := (\omega_1,\omega_2,\omega_3) \in \Omega^3$, the model can finally be cast into the following form: for a final time $T > 0$ we seek the solids volume fraction $u : D_T \times \Omega^3 \to [0,1]$ as the solution of the initial value problem

$$\begin{aligned} u_t(x,t,\boldsymbol{\omega}) + g(x,t,u,\boldsymbol{\omega})_x = 0 \quad &\text{in } D_T \times \Omega^3, \\ u(x,0,\boldsymbol{\omega}) = u_0(x) \quad &\text{for } x \in D, \end{aligned} \tag{5}$$

where the flux function g is determined for $t \in (0,T)$ and $\boldsymbol{\omega} \in \Omega^3$ by

$$g(x,t,u,\boldsymbol{\omega}) = h(x,t,u,\boldsymbol{\omega}) - H(x)\frac{Q_{\mathrm{F}}(t,\omega_2,\omega_3)u_{\mathrm{F}}(t,\omega_1)}{A}.$$

Considering that

$$\frac{Q_{\mathrm{F}}(t,\omega_2,\omega_3)}{A} = q_{\mathrm{R}}(x,t,\omega_3) - q_{\mathrm{L}}(x,t,\omega_2),$$

the flux density function is given by

$$g(x,t,u,\boldsymbol{\omega}) = \begin{cases} (u-u_{\mathrm{F}}(t,\omega_1))q_{\mathrm{L}}(x,t,\omega_2) & \text{for } x < x_{\mathrm{L}}, \\ (u-u_{\mathrm{F}}(t,\omega_1))q_{\mathrm{L}}(x,t,\omega_2) + b(u) & \text{for } x_{\mathrm{L}} < x < 0, \\ (u-u_{\mathrm{F}}(t,\omega_1))q_{\mathrm{R}}(x,t,\omega_3) + b(u) & \text{for } 0 < x < x_{\mathrm{R}}, \\ (u-u_{\mathrm{F}}(t,\omega_1))q_{\mathrm{R}}(x,t,\omega_3) & \text{for } x > x_{\mathrm{R}}. \end{cases} \tag{6}$$

The flux (6) has discontinuities for $x \in \{x_{\mathrm{L}}, 0, x_{\mathrm{R}}\}$. We will not directly work with (5) and the flux (6) but expand the PDE (5) into a system. To this end, we define the flux function

$$f(t,u,\gamma^1,\gamma^2,\boldsymbol{\omega}) := \gamma^1(\omega_2,\omega_3)\big(u - u_{\mathrm{F}}(t,\omega_1)\big) + \gamma^2 b(u),$$

where the vector of unknowns is now $(u,\gamma^1,\gamma^2)^{\mathrm{T}} \in \mathbb{R}\times\mathbb{R}^2$. This vector is a solution to the system of balance laws

$$\begin{aligned} u(x,t,\boldsymbol{\omega})_t + f(t,u,\gamma^1,\gamma^2,\boldsymbol{\omega})_x &= 0, \\ \gamma^1_t(x,t,\omega_2,\omega_3) &= H(x)\big(q_{\mathrm{R}}(x,t,\omega_3) + H(-x)q_{\mathrm{L}}(x,t)\omega_2\big)_t, \\ \gamma^2_t(x,t) &= 0, \end{aligned} \tag{7}$$

subject to the initial conditions

$$\begin{aligned} u(x,0,\boldsymbol{\omega}) &= u_0(x), \\ \gamma^1(x,0,\omega_2,\omega_3) &= H(x)q_{\mathrm{R}}(x,0,\omega_3) + H(-x)q_{\mathrm{L}}(x,0,\omega_2), \\ \gamma^2(x) &= \chi_{(x_{\mathrm{L}},x_{\mathrm{R}})}(x). \end{aligned}$$

3 A hybrid stochastic Galerkin (HSG) finite volume method

3.1 Preliminaries and polynomial chaos

Assume that for a real valued random variable $\theta = \theta(\omega) \in L^2(\Omega)$ on the probability space $(\Omega,\mathcal{P},\mathcal{F})$ its distribution and the corresponding probability density function ρ are known. Then the expectation of θ is given by

$$\mathbf{E}[\theta] := \int_\Omega \theta(\omega)\,\mathrm{d}\mathcal{P}(\omega) = \int_\Omega \theta\,\mathrm{d}\rho(\theta).$$

Let $\{\phi_p(\theta)\}_{p\in\mathbb{N}_0}$ be a family of $L^2(\Omega)$-orthonormal polynomials with respect to ρ, i.e.,

$$\langle \phi_p(\theta),\, \phi_q(\theta)\rangle_{L^2(\Omega)} := \int_\Omega \phi_p\big(\theta(\omega)\big)\,\phi_q\big(\theta(\omega)\big)\,\mathrm{d}\mathcal{P}(\omega) = \delta_{p,q} \quad \text{for } p,q \in \mathbb{N}_0. \tag{8}$$

Here $\delta_{p,q}$ denotes the Kronecker symbol. Of course, the choice of the polynomials ϕ_p depends on ρ. For example, Hermite polynomials are required for a Gauss distribution, and Legendre polynomials allow us to use the approach of uniformly distributed random variables. For definitions of the polynomials and their properties we refer to [31].

Let (with a slight abuse of notation) $w = w(x,t,\omega) = w(x,t,\theta(\omega))$, $(x,t) \in D_T$, be a random variable with finite variance for each $(x,t) \in D_T$. Then w can be represented by the series

$$w\big(x,t,\theta(\omega)\big) = \sum_{p=0}^{\infty} w^p(x,t)\phi_p\big(\theta(\omega)\big), \quad (x,t) \in D_T.$$

Here the coefficients $w^p = w^p(x,t)$ are defined by

$$w^p := \langle w,\, \phi_p\rangle_{L^2(\Omega)} = \int_\Omega w\big(\theta(\omega)\big)\phi_p\big(\theta(\omega)\big)\,\mathrm{d}\mathcal{P}\,(\omega) \;\text{ for } p \in \mathbb{N}_0.$$

Note that the expectation of the random field w is given by the coefficient w^0 and its variance is given by the series $\sum_{p=1}^{\infty}(w^p)^2$. The truncation at the highest polynomial order $N_\mathrm{o} \in \mathbb{N}$ yields a finite sum, namely

$$\mathit{\Pi}^{N_\mathrm{o}}\,[w]\,\big(x,t,\theta(\omega)\big) := \sum_{p=0}^{N_\mathrm{o}} w^p(x,t)\phi_p\big(\theta(\omega)\big), \quad (x,t) \in D_T.$$

The Cameron-Martin theorem [14,37] ensures convergence of this series, i.e., $\mathit{\Pi}^{N_\mathrm{o}}\,[w] \to w$ in $L^2(\Omega)$ for $N_\mathrm{o} \to \infty$. For further reading we refer to [23,30,32].

3.2 Extension to several stochastic dimensions

To extend the discussion from a one-dimensional stochastic discretization to that of N stochastic dimensions, let us consider a vector $\theta(\boldsymbol{\omega}) := \{\theta_1(\omega_1), \dots \theta_N(\omega_N)\}$. We assume that the random variables θ_i, $i = 1,\dots,N$, are i.i.d. (independent identically distributed). For a multi-index $\mathfrak{p} \in \mathbb{N}_0^N$, $\mathfrak{p} = (\mathfrak{p}_1, \cdots, \mathfrak{p}_N)$, we define a multivariate polynomial

$$\mathit{\Phi}_\mathfrak{p}(\theta) := \phi_{\mathfrak{p}_1}(\theta_1) \cdot \ldots \cdot \phi_{\mathfrak{p}_N}(\theta_N).$$

The family of multivariate polynomials $\{\mathit{\Phi}_\mathfrak{p}\}_{\mathfrak{p}\in\mathbb{N}_0^N}$ defined in this way is orthonormal with respect to the standard scalar product of $L^2(\Omega_1 \times \ldots \times \Omega_N)$, i.e.,

$$\langle \mathit{\Phi}_\mathfrak{p},\, \mathit{\Phi}_\mathfrak{q}\rangle_{L^2(\Omega_1\times\cdots\times\Omega_N)} := \int_{\Omega_1}\cdots\int_{\Omega_N} \mathit{\Phi}_\mathfrak{p}(\theta(\boldsymbol{\omega}))\mathit{\Phi}_\mathfrak{q}(\theta(\boldsymbol{\omega}))\,\mathrm{d}\mathcal{P}_N(\omega_N)\cdots\mathrm{d}\mathcal{P}_1(\omega_1) = \delta_{\mathfrak{p},\mathfrak{q}}, \quad (9)$$

for $\mathfrak{p},\mathfrak{q} \in \mathbb{N}_0^N$. Here $\delta_{\mathfrak{p},\mathfrak{q}}$ denotes the Kronecker symbol. In what follows, we limit the discussion to the case $\Omega_1 = \ldots = \Omega_N =: \Omega$ and $\mathcal{P}_1 = \ldots = \mathcal{P}_N =: \mathcal{P}$, for which we may simplify notation; for instance, (9) can be expressed as

$$\langle \mathit{\Phi}_\mathfrak{p},\, \mathit{\Phi}_\mathfrak{q}\rangle_{L^2(\Omega^N)} := \int_{\Omega^N} \mathit{\Phi}_\mathfrak{p}(\theta(\boldsymbol{\omega}))\mathit{\Phi}_\mathfrak{q}(\theta(\boldsymbol{\omega}))\,\mathrm{d}\mathcal{P}(\boldsymbol{\omega}) = \delta_{\mathfrak{p},\mathfrak{q}}.$$

Let $w = w(x,t,\theta(\boldsymbol{\omega}))$, $(x,t) \in D_T$, $\boldsymbol{\omega} \in \Omega^N$ be a random variable with finite variance. The PC expansion of w is given by

$$w\big(x,t,\theta(\boldsymbol{\omega})\big) = \sum_{p=0}^{\infty}\sum_{|\mathfrak{p}|=p} w^\mathfrak{p}(x,t)\mathit{\Phi}_\mathfrak{p}(\theta), \quad (x,t) \in D_T.$$

Here the coefficients $w^{\mathfrak{p}}$ for $\mathfrak{p} \in \mathbb{N}_0^N$ are given by $w^{\mathfrak{p}} := \langle w, \Phi_{\mathfrak{p}} \rangle_{L^2(\Omega_1 \times \cdots \times \Omega_N)}$, and the order $|\mathfrak{p}|$ of the multi-index $\mathfrak{p}$ is defined by $|\mathfrak{p}| := \sum_{i=1}^N |\mathfrak{p}_i|$. The truncation at the highest polynomial order $|\mathfrak{p}| = N_\mathrm{o} \in \mathbb{N}_0$ yields a finite sum denoted by $\mathit{\Pi}^{N_\mathrm{o}}[w]$, namely

$$\mathit{\Pi}^{N_\mathrm{o}}[w]\big(x,t,\theta(\boldsymbol{\omega})\big) := \sum_{|\mathfrak{p}|=0}^{N_\mathrm{o}} w^{\mathfrak{p}}(x,t)\Phi_{\mathfrak{p}}\big(\theta(\boldsymbol{\omega})\big), \quad (x,t) \in D_T, \quad \boldsymbol{\omega} \in \Omega^N.$$

Here and in what follows, we use for summands $s^{\mathfrak{p}}$, $\mathfrak{p} = (\mathfrak{p}_1, \ldots, \mathfrak{p}_N) \in \mathbb{N}_0^N$, the notation

$$\sum_{|\mathfrak{p}|=0}^{N_\mathrm{o}} s^{\mathfrak{p}} := \sum_{k=0}^{N_\mathrm{o}} \sum_{\mathfrak{p}=(\mathfrak{p}_1,\ldots,\mathfrak{p}_N):|\mathfrak{p}|=k} s^{\mathfrak{p}}.$$

For later use we remark that the total number of terms in this sum is $P+1$, where we define

$$P := \frac{(N_\mathrm{o}+N)!}{N_\mathrm{o}!N!} - 1. \tag{10}$$

The expectation and variance of the truncated random field $\mathit{\Pi}^{N_\mathrm{o}} w$ are given by

$$\mathbf{E}\,\mathit{\Pi}^{N_\mathrm{o}}[w] = \Big\langle \mathit{\Pi}^{N_\mathrm{o}}[w]\,,\,\Phi_0 \Big\rangle = w^0,$$

$$\mathbf{Var}\,\mathit{\Pi}^{N_\mathrm{o}}[w] = \Big\langle \Big(\mathit{\Pi}^{N_\mathrm{o}}[w] - w^0\Big)^2\,,\,\Phi_0 \Big\rangle = \sum_{|\mathfrak{p}|=1}^{N_\mathrm{o}} (w^{\mathfrak{p}})^2.$$

3.3 The stochastic Galerkin finite volume (SG-FV) method

Similarly to the treatment in [13] we apply the PC framework to the governing model. The resulting non-strictly hyperbolic system [9] allows us to use appropriate finite volume methods. Note that we have in this section $N = 3$.

3.3.1 Formulation of the stochastic Galerkin system

Multiplying the governing equation (7) by the multivariate polynomial $\Phi_{\mathfrak{p}}$, $|\mathfrak{p}| = 0, \ldots, N_\mathrm{o}$ and integrating the result over Ω_3 we obtain the system

$$\int_{\Omega_3} \Big(u_t(x,t,\boldsymbol{\omega}) + \big(\gamma^1(x,t,\omega_2,\omega_3)\big(u(x,t,\boldsymbol{\omega}) - u_\mathrm{F}(t,\omega_1)\big) + \gamma^2(x) b\big(u(x,t,\boldsymbol{\omega})\big)\big)_x \Big) \Phi_{\mathfrak{p}}(\boldsymbol{\omega})\,\mathrm{d}\mathcal{P}(\boldsymbol{\omega}) = 0 \quad \text{for } |\mathfrak{p}| = 0, \ldots, N_\mathrm{o}.$$

For ease of notation we keep here a strong formulation in the deterministic variables. We replace $u(x,t,\boldsymbol{\omega})$, $u_\mathrm{F}(t,\omega_1)$, $\gamma^1(x,t,\omega_2,\omega_3)$ by their truncated PC expansions

$$\mathit{\Pi}^{N_\mathrm{o}}[u]\,(x,t,\boldsymbol{\omega}) = \sum_{|\mathfrak{p}|=0}^{N_\mathrm{o}} u^{\mathfrak{p}}(x,t)\Phi_{\mathfrak{p}}(\boldsymbol{\omega}),$$

$$\mathit{\Pi}^{N_\mathrm{o}}[u_\mathrm{F}]\,(t,\boldsymbol{\omega}) = \sum_{|\mathfrak{p}|=0,}^{N_\mathrm{o}} u_\mathrm{F}^{\mathfrak{p}}(t)\Phi_{\mathfrak{p}}(\boldsymbol{\omega}),$$

$$\mathit{\Pi}^{N_\mathrm{o}}\left[\gamma^1\right](x,t,\boldsymbol{\omega}) = \sum_{|\mathfrak{p}|=0}^{N_\mathrm{o}} (\gamma^1)^{\mathfrak{p}}(x,t)\Phi_{\mathfrak{p}}\big(\boldsymbol{\omega}\big).$$

Since $u_{\mathrm{F}}(\omega_1)$ is independent of ω_2 and ω_3 and $\gamma^1(x,t,\omega_2,\omega_3)$ is independent of ω_1, we obtain $u_{\mathrm{F}}^{\mathfrak{p}}=0$ for $\mathfrak{p}_2\neq 0,\mathfrak{p}_3\neq 0$ and $(\gamma^1)^{\mathfrak{p}}=0$ for $\mathfrak{p}_1\neq 0$. This property can be used for the reduction of the computational effort.

Using now the orthogonality relation (8) we obtain the truncated **SG system** for the coefficients $u^{\mathfrak{p}}$, $|\mathfrak{p}|=0,\dots,N_{\mathrm{o}}$.

$$u_t^{\mathfrak{p}}+ \partial_x\left\langle\left(\sum_{|\mathfrak{q}|=0}^{N_{\mathrm{o}}}(u^{\mathfrak{q}}-u_{\mathrm{F}}^{\mathfrak{q}})\Phi_{\mathfrak{q}}\right)\sum_{|\mathfrak{q}|=0}^{N_{\mathrm{o}}}(\gamma^1)^{\mathfrak{q}}\Phi_{\mathfrak{q}}+\gamma^2 b\left(\sum_{|\mathfrak{q}|=0}^{N_{\mathrm{o}}}u^{\mathfrak{q}}\Phi_{\mathfrak{q}}\right),\Phi_{\mathfrak{p}}\right\rangle_{L^2(\Omega^3)}=0. \quad (11)$$

Finally, from (11) and the additional equations for γ^1 and γ^2 we obtain a strictly hyperbolic system (cf. [36,9]).

3.3.2 Finite volume method

The system (11) is quite general and it appears hard to construct e.g. a Godunov-type solver without further analytical knowledge. Furthermore, the common upwind-biased Engquist-Osher flux [22], which is usually applied for scalar problems with discontinuous flux [5–7], cannot be used for the higher-dimensional SG-system (11) since spectral information on the Jacobian of the flux vector involved is difficult to obtain or unavailable. Therefore, at least for the computations in one space dimension, as in [13], we use the simple Lax-Friedrichs method on a uniform mesh with cells $[x_{i-1/2},x_{i+1/2})$, $i\in\mathbb{Z}$ and $\Delta x=x_{i+1/2}-x_{i-1/2}$. Restricting ourselves to the $P+1$ u-components $u^{\mathfrak{q}}$ for $|\mathfrak{q}|=0,\dots,N_{\mathrm{o}}$, we have for a time step $\Delta t^n>0$ the following SG-FV scheme:

$$\begin{aligned}
u_i^{\mathfrak{p},n+1} =& u_i^{\mathfrak{p},n}-\frac{\Delta t^n}{\Delta x}\left(F_{i+1/2}^{\mathfrak{p},n}-F_{i-1/2}^{\mathfrak{p},n}\right) \qquad (i\in\mathbb{Z},\ n\in\mathbb{N},\ |\mathfrak{p}|=0,\dots,N_{\mathrm{o}}),\\
F_{i+1/2}^{\mathfrak{p},n} :=& \frac{1}{2}\Big(f^{\mathfrak{p}}\big(t^n,\{u_i^{\mathfrak{q},n}\}_{|\mathfrak{q}|\le N_{\mathrm{o}}},\{(\gamma^1)_i^{\mathfrak{q},n}\}_{|\mathfrak{q}|\le N_{\mathrm{o}}},(\gamma^2)_i^n\big)\\
&\quad + f^{\mathfrak{p}}\big(t^n,\{u_{i+1}^{\mathfrak{q},n}\}_{|\mathfrak{q}|\le N_{\mathrm{o}}},\{(\gamma^1)_{i+1}^{\mathfrak{q},n}\}_{|\mathfrak{q}|\le N_{\mathrm{o}}},(\gamma^2)_{i+1}^n\big)\Big)\\
&\quad + \frac{\Delta x}{2\Delta t^n}\left(u_{i+1}^{\mathfrak{p},n}-u_i^{\mathfrak{p},n}\right).
\end{aligned}$$

The function $f^{\mathfrak{p}}$ for $|\mathfrak{p}|=0,\dots,N_{\mathrm{o}}$ is defined by

$$\begin{aligned}
&f^{\mathfrak{p}}\big(t,\{u^{\mathfrak{q},n}\}_{|\mathfrak{q}|\le N_{\mathrm{o}}},\{(\gamma^1)^{\mathfrak{q},n}\}_{|\mathfrak{q}|\le N_{\mathrm{o}}},(\gamma^2)^n\big)\\
&:=\left\langle\sum_{|\mathfrak{q}|=0}^{N_{\mathrm{o}}}(\gamma^1)^{\mathfrak{q}}\Phi_{\mathfrak{q}}\left(\sum_{|\mathfrak{q}|=0}^{N_{\mathrm{o}}}(u^{\mathfrak{q}}-u_{\mathrm{F}}^{\mathfrak{q}})\Phi_{\mathfrak{q}}\right)+\gamma^2 b\left(\sum_{|\mathfrak{q}|=0}^{N_{\mathrm{o}}}u^{\mathfrak{q}}\Phi_{\mathfrak{q}}\right),\Phi_{\mathfrak{p}}\right\rangle_{L^2(\Omega^3)}.
\end{aligned}$$

Initial values are obtained from $u_i^{0,0}=u_0$ and setting all other components equal to zero.

3.4 A hybrid stochastic Galerkin (HSG) finite volume method

The SG-FV method defined in Section 3.3.2 permits fast and accurate computations for a small maximal polynomial order N_{o}. Increasing N_{o} will significantly increase the computational effort and the synchronisation costs that slow down computations. The HSG method

to be introduced in this section allows us to reduce the maximal polynomial order N_o and to obtain a partially decoupled system of equations. This property decreases the synchronisation effort of the parallel computation considerably, and permits efficient parallel computing on distributed memory machines.

3.4.1 Stochastic discretization

To focus on the main idea, let us concentrate for the moment on one single stochastic dimension (as in [9]) before passing to several stochastic dimensions. Let $\theta = \theta(\omega) \in L^2(\Omega)$ be a random variable on the probability space $(\Omega, \mathcal{P}, \mathcal{F})$. For sake of brevity we assume that θ is uniformly distributed on the interval $[0,1]$, denoted by $\theta \sim \mathcal{U}(0,1)$. The main idea of the method is the dyadical decomposition of the stochastic domain $[0,1]$. For $N_\mathrm{o} \in \mathbb{N}_0$ and $N_\mathrm{r} \in \mathbb{N}_0$ we define the interval

$$I_l^{N_\mathrm{r}} := [2^{-N_\mathrm{r}} l, 2^{-N_\mathrm{r}}(l+1)] \quad \text{for } l = 0, \dots, 2^{N_\mathrm{r}} - 1, \tag{12}$$

and the following space of piecewise polynomial functions $S^{N_\mathrm{o},\,N_\mathrm{r}}$:

$$S^{N_\mathrm{o},\,N_\mathrm{r}} := \left\{ w : [0,1] \to \mathbb{R} \;\middle|\; w|_{I_l^{N_\mathrm{r}}} \in \mathbb{Q}_{N_\mathrm{o}}[\theta],\ \forall\, l \in \{0, \dots, 2^{N_\mathrm{r}} - 1\} \right\}. \tag{13}$$

Here $\mathbb{Q}_{N_\mathrm{o}}[\theta]$ denotes the space of real polynomials in θ with maximal degree N_o. The vector space $S^{N_\mathrm{o},\,N_\mathrm{r}}$ has the dimension $2^{N_\mathrm{r}}(N_\mathrm{o}+1)$. Note that the vector space $S^{N_\mathrm{o},\,0}$ corresponds to the PC approach introduced in Section 3.1. The basis of $S^{N_\mathrm{o},\,0}$ can be given by rescaled Legendre polynomials ϕ_p, $p = 0, \dots, N_\mathrm{o}$, such that

$$\left\langle \phi_p(\theta(\omega_1)), \phi_q(\theta(\omega_1)) \right\rangle_{L^2(\Omega)} = \delta_{p,q} \quad \text{for } 0 \le p, q \le N_\mathrm{o}. \tag{14}$$

The space $S^{N_\mathrm{o},\,N_\mathrm{r}}$ is spanned by the polynomials $\phi_{p,l}^{N_\mathrm{r}}$ defined by

$$\phi_{p,l}^{N_\mathrm{r}}(\xi) = \begin{cases} 2^{N_\mathrm{r}/2} \phi_p(2^{N_\mathrm{r}} \xi - l) & \text{for } \xi \in I_l^{N_\mathrm{r}}, \\ 0 & \text{otherwise} \end{cases}$$

$$\text{for } p = 0, \dots, N_\mathrm{o} \text{ and } l = 0, \dots, 2^{N_\mathrm{r}} - 1.$$

The polynomials $\phi_{p,l}^{N_\mathrm{r}}$ satisfy the orthogonality relation

$$\left\langle \phi_{p,l}^{N_\mathrm{r}}(\theta(\omega_1)), \phi_{q,k}^{N_\mathrm{r}}(\theta(\omega_1)) \right\rangle_{L^2(\Omega)} = \delta_{p,q}\delta_{k,l} \quad \text{for } 0 \le p, q \le N_\mathrm{o} \text{ and } 0 \le k, l \le 2^{N_\mathrm{r}} - 1.$$

Let w be a random variable that satisfies $w(x,t,\theta(\cdot)) \in L^2(\Omega)$, $x \in D_T$, $t \in [0,T]$. The projection $\mathit{\Pi}^{N_\mathrm{o},N_\mathrm{r}} : L^2(\Omega) \to S^{N_\mathrm{o},\,N_\mathrm{r}}$ is defined by

$$\begin{aligned} \mathit{\Pi}^{N_\mathrm{o},N_\mathrm{r}}[w](x,t,\theta) &:= \sum_{l=0}^{2^{N_\mathrm{r}}-1} \sum_{p=0}^{N_\mathrm{o}} \left\langle w(x,t,\theta), \phi_{p,l}^{N_\mathrm{r}} \right\rangle_{L^2(\Omega)} \phi_{p,l}^{N_\mathrm{r}}(\theta) \\ &= \sum_{l=0}^{2^{N_\mathrm{r}}-1} \sum_{p=0}^{N_\mathrm{o}} w_{p,l}^{N_\mathrm{r}}(x,t) \phi_{p,l}^{N_\mathrm{r}}(\theta). \end{aligned}$$

Here the coefficients $w_{p,l}^{N_\mathrm{r}}$ are given by

$$w_{p,l}^{N_\mathrm{r}} := \left\langle w, \phi_{p,l}^{N_\mathrm{r}} \right\rangle_{L^2(\Omega)} \quad \text{for } 0 \le p \le N_\mathrm{o} \text{ and } 0 \le l \le 2^{N_\mathrm{r}} - 1.$$

For the approximation property of the projection $\mathit{\Pi}^{N_\mathrm{o},N_\mathrm{r}}$ for $N_\mathrm{o},\ N_\mathrm{r} \to \infty$ we refer to [3]. The expectation and variance of the projection $\mathit{\Pi}^{N_\mathrm{o},N_\mathrm{r}}[w]$ can be computed by

$$\mathbf{E}\left[\mathit{\Pi}^{N_\mathrm{o},N_\mathrm{r}}[w](x,t)\right] := \sum_{l=0}^{2^{N_\mathrm{r}}-1}\sum_{p=0}^{N_\mathrm{o}} w_{p,l}^{N_\mathrm{r}}(x,t)\left\langle \phi_{p,l}^{N_\mathrm{r}}, \phi_{0,0}^{0}\right\rangle_{L^2(\Omega)},$$

$$\begin{aligned}\mathbf{Var}\left[\mathit{\Pi}^{N_\mathrm{o},N_\mathrm{r}}[w](x,t)\right] := &\sum_{l=0}^{2^{N_\mathrm{r}}-1}\sum_{p=0}^{N_\mathrm{o}}\sum_{q=0}^{N_\mathrm{o}} w_{p,l}^{N_\mathrm{r}}(x,t)w_{q,l}^{N_\mathrm{r}}(x,t)\left\langle \phi_{p,l}^{N_\mathrm{r}}\phi_{q,l}^{N_\mathrm{r}}, \phi_{0,0}^{0}\right\rangle_{L^2(\Omega)}\\ &- \left(\mathbf{E}\left[\mathit{\Pi}^{N_\mathrm{o},N_\mathrm{r}}[w](x,t)\right]\right)^2.\end{aligned}$$

If $w \sim \mathcal{U}(0,1)$, then we have $\phi_{0,0}^0 \equiv 1$. Together with the orthogonality of $\phi_{q,l}^{N_\mathrm{r}}$, $q = 0,\dots,N_\mathrm{o}, l = 0,\dots,2^{N_\mathrm{r}}-1$ this implies

$$\mathbf{Var}\left[\mathit{\Pi}^{N_\mathrm{o},N_\mathrm{r}}[w](x,t)\right] := \sum_{l=0}^{2^{N_\mathrm{r}}-1}\sum_{p=0}^{N_\mathrm{o}}\left(w_{p,l}^{N_\mathrm{r}}(x,t)\right)^2 - \left(\mathbf{E}\left[\mathit{\Pi}^{N_\mathrm{o},N_\mathrm{r}}[w](x,t)\right]\right)^2.$$

3.4.2 Extension to several stochastic dimensions

Let us consider an N-dimensional i.i.d. random vector $\theta(\boldsymbol{\omega}) := \{\theta_1(\omega_1),\dots\theta_N(\omega_N)\}$ that satisfies $\theta(\boldsymbol{\omega}) \in L^2(\Omega^N)$. We assume that $\theta_i \sim \mathcal{U}(0,1)$ for $i = 1,\dots,N$. (Other choices of the distribution or the interval are possible by an appropriate choice of the polynomial base.) The stochastic domain Ω^N is decomposed into 2^{NN_r} stochastic elements

$$\begin{aligned}I_{N,l}^{N_\mathrm{r}} &:= I_{l_1}^{N_\mathrm{r}} \times \cdots \times I_{l_N}^{N_\mathrm{r}},\\ &l = (l_1,\dots,l_N) \in \mathcal{I} = \tilde{\mathcal{I}}^N, \quad \tilde{\mathcal{I}} := \{0,1,\dots,2^{N_\mathrm{r}}-1\}, \quad (15)\end{aligned}$$

where the one-dimensional intervals $I_{l_i}^{N_\mathrm{r}}$ are defined in (12). In the multivariate case, the definition (13) of the space of piecewise polynomial functions $S^{N_\mathrm{o},\,N_\mathrm{r}}$ is replaced by

$$S_N^{N_\mathrm{o},\,N_\mathrm{r}} := \left\{ w : [0,1]^N \to \mathbb{R} \;\middle|\; w|_{I_{N,l}^{N_\mathrm{r}}} \in \mathbb{Q}_{N_\mathrm{o}}^N[\theta],\ \forall\, l \in \mathcal{I} \right\}.$$

Here $\mathbb{Q}_{N_\mathrm{o}}^N[\theta]$ denotes the space of N-variate polynomials of degree $|\mathfrak{p}| \le N_\mathrm{o}$.

The vector space $S_N^{N_\mathrm{o},\,0}$ corresponds to the multivariate PC expansion introduced in Section 3.2. Thus, its basis may be given by the N-variate polynomials $\{\Phi_\mathfrak{p}\}_{\mathfrak{p}\in\mathbb{N}_0^N,|\mathfrak{p}|\le N_\mathrm{o}}$. The space $S_N^{N_\mathrm{o},\,N_\mathrm{r}}$ is spanned by the polynomials $\Phi_{\mathfrak{p},l}^{N_\mathrm{r}}$ defined by

$$\Phi_{\mathfrak{p},l}^{N_\mathrm{r}}(\theta) := \begin{cases} 2^{NN_\mathrm{r}/2}\displaystyle\prod_{k=1}^{N}\phi_{\mathfrak{p}_k}(2^{N_\mathrm{r}}\theta_k - l_k) & \text{for } \theta \in I_{N,l}^{N_\mathrm{r}},\\ 0 & \text{otherwise,}\end{cases} \quad (16)$$

$$\mathfrak{p} \in \mathbb{N}_0^N,\ |\mathfrak{p}| \le N_\mathrm{o},\ l \in \mathcal{I}.$$

These polynomials satisfy the orthogonality relation

$$\left\langle \Phi_{\mathfrak{p},l}^{N_\mathrm{r}}, \Phi_{\mathfrak{q},k}^{N_\mathrm{r}}\right\rangle_{L^2(\Omega^N)} = \delta_{\mathfrak{p},\mathfrak{q}}\delta_{l,k} \quad \text{for } \mathfrak{p},\mathfrak{q} \in \mathbb{N}_0^N, |\mathfrak{p}|, |\mathfrak{q}| \le N_\mathrm{o}, \text{ and } l \in \mathcal{I}. \quad (17)$$

For the random field $w(\theta(\boldsymbol{\omega})) \in L^2(\Omega^N)$ and $(x,t) \in D_T$, we define the projection $\Pi^{N_\mathrm{o},N_\mathrm{r}} : L^2(\Omega^N) \to S_N^{N_\mathrm{o},N_\mathrm{r}}$ by

$$\Pi^{N_\mathrm{o},N_\mathrm{r}}[w](x,t,\theta) := \sum_{l\in\mathcal{I}} \sum_{|\mathfrak{p}|=0}^{N_\mathrm{o}} w_{\mathfrak{p},l}^{N_\mathrm{r}}(x,t)\Phi_{\mathfrak{p},l}^{N_\mathrm{r}}(\theta).$$

Here the coefficients $w_{\mathfrak{p},l}^{N_\mathrm{r}}$ are given by

$$w_{\mathfrak{p},l}^{N_\mathrm{r}} = \left\langle w, \Phi_{\mathfrak{p},l}^{N_\mathrm{r}} \right\rangle_{L^2(\Omega_N)} \quad \text{for } 0 \le |\mathfrak{p}| \le N_\mathrm{o} \text{ and } l \in \mathcal{I}.$$

For the approximation property of the projection $\Pi^{N_\mathrm{o},N_\mathrm{r}}$ for $N_\mathrm{o},\ N_\mathrm{r} \to \infty$ we refer to [3]. The expectation and variance of $\Pi^{N_\mathrm{o},N_\mathrm{r}}[w]$ can be directly computed as follows:

$$\mathbf{E}\left[\Pi^{N_\mathrm{o},N_\mathrm{r}}[w](x,t)\right] := \sum_{l\in\mathcal{I}} \sum_{|\mathfrak{p}|=0}^{N_\mathrm{o}} w_{\mathfrak{p},l}^{N_\mathrm{r}}(x,t)\left\langle \Phi_{\mathfrak{p},l}^{N_\mathrm{r}}, \Phi_{0,0}^{0}\right\rangle_{L^2(\Omega_N)},$$

$$\begin{aligned}\mathbf{Var}\left[\Pi^{N_\mathrm{o},N_\mathrm{r}}[w](x,t)\right] := &\sum_{l\in\mathcal{I}} \sum_{|\mathfrak{p}|=0}^{N_\mathrm{o}} \sum_{|\mathfrak{q}|=0}^{N_\mathrm{o}} w_{\mathfrak{p},l}^{N_\mathrm{r}}(x,t) w_{\mathfrak{q},l}^{N_\mathrm{r}}(x,t)\left\langle \Phi_{\mathfrak{p},l}^{N_\mathrm{r}}\Phi_{\mathfrak{q},l}^{N_\mathrm{r}}, \Phi_{0,0}^{0}\right\rangle_{L^2(\Omega_N)} \\ &- \left(\mathbf{E}\left[\Pi^{N_\mathrm{o},N_\mathrm{r}}[w](x,t)\right]\right)^2.\end{aligned}$$

(In the case that the random field w is uniformly distributed on $[0,1]^N$, we have $\phi_{0,0}^0 \equiv 1$.) In light of the orthogonality relation (17), we obtain

$$\mathbf{E}\left[\Pi^{N_\mathrm{o},N_\mathrm{r}}[w](x,t)\right] = \sum_{l=0}^{2^{NN_\mathrm{r}}-1} w_{0,l}^{N_\mathrm{r}}(x,t)\left\langle \Phi_{0,l}^{N_\mathrm{r}}, \Phi_{0,0}^{0}\right\rangle_{L^2(\Omega_N)},$$

$$\mathbf{Var}\left[\Pi^{N_\mathrm{o},N_\mathrm{r}}[w](x,t)\right] = \sum_{l=0}^{2^{NN_\mathrm{r}}-1} \sum_{|\mathfrak{p}|=0}^{N_\mathrm{o}} \left(w_{\mathfrak{p},l}^{N_\mathrm{r}}(x,t)\right)^2 - \left(\mathbf{E}\left[\Pi^{N_\mathrm{o},N_\mathrm{r}}[w](x,t)\right]\right)^2.$$

3.4.3 Application of the hybrid stochastic Galerkin approach to the clarifier-thickener model

We now apply the stochastic discretization introduced above to the governing equation (7), where we recall that $N = 3$ under the present assumptions. The basic idea is to replace the stochastically perturbed parameters u_F and γ^1 and the unknown solution u by their respective projections onto $S^{N_\mathrm{r},\,N_\mathrm{o}}$, denoted by $\Pi^{N_\mathrm{o},N_\mathrm{r}}[u_\mathrm{F}]$, $\Pi^{N_\mathrm{o},N_\mathrm{r}}\left[\gamma^1\right]$ and $\Pi^{N_\mathrm{o},N_\mathrm{r}}[u]$, respectively, and to compute the coefficients $u_{\mathfrak{p},l}^{N_\mathrm{r}}$ of $\Pi^{N_\mathrm{o},N_\mathrm{r}}[u]$ for $|\mathfrak{p}| \le N_\mathrm{o}$ and $l \in \mathcal{I}$.

We now assume that $N, N_\mathrm{r}, N_\mathrm{o} \in \mathbb{N}_0$ are fixed, and define for ease of notation

$$\Pi := \Pi^{N_\mathrm{r},N_\mathrm{o}}.$$

Then the **HSG approach** (for the first equation in (7)) reads as follows:

find coefficients $u_{\mathfrak{q},k}^{N_\mathrm{r}} : D_T \to \mathbb{R}$ for all $|\mathfrak{q}| \le N_\mathrm{o}$ and $k \in \mathcal{I}$ such that

$$\int_{\Omega_3} \left(\Pi[u]_t + \left(\left(\Pi[u] - \Pi[u_\mathrm{F}]\right)\Pi[\gamma^1] + \gamma^2 b\left(\Pi[u]\right)\right)_x\right)\Phi_{\mathfrak{p},l}^{N_\mathrm{r}}\,\mathrm{d}\mathcal{P}(\boldsymbol{\omega}) = 0 \qquad (18)$$

for all $|\mathfrak{p}| \le N_\mathrm{o}$ and $l \in \mathcal{I}$.

Since by (16)

$$\operatorname{supp} \Phi_{\mathfrak{p},l}^{N_\mathrm{r}} \subseteq I_{N,l}^{N_\mathrm{r}} \quad \text{for all } |\mathfrak{p}| \leq N_\mathrm{o} \text{ and } l \in \mathcal{I},$$

the system is decoupled in the stochastic element index l. This property is fundamental for parallel computing.

For the convenient discussion of the final HSG-FV scheme we replace the index pair $(\mathfrak{p}, l)$ by $\alpha \in \{0, 1, \ldots, M-1\}$, where

$$M := \dim S_N^{N_\mathrm{o},\, N_\mathrm{r}} = (P+1)2^{NN_\mathrm{r}} = \frac{(N_\mathrm{o}+N)!}{N_\mathrm{o}!N!} 2^{NN_\mathrm{r}}$$

(see (10)). Then (18) can be compactly written in the following form:

find coefficients $u_0^{N_\mathrm{r}}, \ldots, u_{M-1}^{N_\mathrm{r}} : D_T \to \mathbb{R}$ for all $|\mathfrak{p}| \leq N_\mathrm{o}$ and $l \in \mathcal{I}$ such that

$$\int_\Omega \Big(\mathit{\Pi}[u]_t + \Big((\mathit{\Pi}[u] - \mathit{\Pi}[u_\mathrm{F}])\, \mathit{\Pi}[\gamma^1] + \gamma^2 b\,(\mathit{\Pi}[u]) \Big)_x \Big) \Phi_\alpha^{N_\mathrm{r}} \,\mathrm{d}\mathcal{P}(\boldsymbol{\omega}) = 0 \tag{19}$$

for all $\alpha = 0, \ldots, M-1$.

For the given stochastically one-dimensional approximation of $u_\mathrm{F}(t, \omega_1)$ we employ the notation

$$\mathit{\Pi}[u_\mathrm{F}](t, \omega_1) \equiv \mathit{\Pi}^{N_\mathrm{o}, N_\mathrm{r}}\,[u_\mathrm{F}]\,(t, \omega_1),$$

and the stochastic approximation of $\gamma^1(x, t, \omega_2, \omega_3)$ is denoted by

$$\mathit{\Pi}[\gamma^1](x, t, \omega_2, \omega_3) \equiv \mathit{\Pi}^{N_\mathrm{o}, N_\mathrm{r}} \left[\gamma^1\right] (x, t, \omega_2, \omega_3).$$

Using now the orthogonality from (14), we can rewrite (19) in the following form:

$$u_t^\alpha + \Big(\Big\langle \mathit{\Pi}[\gamma^1]\,(\mathit{\Pi}[u] - \mathit{\Pi}[u_\mathrm{F}]) + \gamma^2 b\,(\mathit{\Pi}[u])\,,\, \Phi_\alpha^{N_\mathrm{r}} \Big\rangle_{L^2(\Omega_3)} \Big)_x = 0, \qquad \alpha = 0, \ldots, M-1. \tag{20}$$

With the method introduced in [36,9] we finally obtain from (20) an $(M+2)$-dimensional system for the determination of the unknown u. Using the (non-strict) hyperbolicity of (7) and the decoupled structure it can be shown that this system (20) is non-strictly hyperbolic [9].

The system (20) is decoupled in the stochastic element index $l \in \mathcal{I}$. This allows the efficient parallelisation on the distributed memory machines since the synchronisation between decoupled nodes can be omitted.

3.4.4 Finite volume method

Similarly to the SG approach of Section 3.3.2 we use the Lax-Friedrichs scheme on a uniform mesh with cells $[x_{i-1/2}, x_{i+1/2})$, $i \in \mathbb{Z}$ and $\Delta x = x_{i+1/2} - x_{i-1/2}$ for the computations in one space dimension. As mentioned above, the common upwind-biased Engquist-Osher flux [22] to scalar problems with discontinuous flux [5–7] cannot be used for the higher–dimensional stochastic Galerkin system. Restricting ourselves to the u-components

$u^0, \dots, u^{M-1}$ we have for the time step $\Delta t^n > 0$ the following HSG-FV scheme adapted to the CT model:

$$u_i^{\alpha,n+1} = u_i^{\alpha,n} - \frac{\Delta t^n}{\Delta x}\left(F_{i+1/2}^{\alpha,n} - F_{i-1/2}^{\alpha,n}\right) \qquad (i \in \mathbb{Z},\, n \in \mathbb{N},\, \alpha = 0, \dots, M-1),$$

$$\begin{aligned} F_{i+1/2}^{\alpha,n} := \frac{1}{2}\Big(& f^\alpha\left(t^n, u_i^{0,n}, \dots, u_i^{M-1,n}, (\gamma^1)_i^{0,n}, \dots, (\gamma^1)_i^{M-1,n}, (\gamma^2)_i^n\right) \\ & + f^\alpha\left(t^n, u_{i+1}^{0,n}, \dots, u_{i+1}^{M-1,n}, (\gamma^1)_{i+1}^{0,n}, \dots, (\gamma^1)_{i+1}^{M-1,n}, (\gamma^2)_{i+1}^n\right)\Big) \\ & + \frac{\Delta x}{2\Delta t^n}\left(u_i^{\alpha,n} - u_{i+1}^{\alpha,n}\right). \end{aligned}$$

The function f^α for $\alpha = 0, \dots, M-1$ is defined by

$$\begin{aligned} & f^\alpha\left(t, u^0, \dots, u^{M-1}, (\gamma^1)^0, \dots, (\gamma^1)^{M-1}, \gamma^2\right) \\ & := \left\langle \Pi[\gamma^1]\left(\Pi[u] - \Pi[u_{\mathrm{F}}]\right) + \gamma^2 b\left(\Pi[u]\right),\, \Phi_\alpha \right\rangle_{L^2(\Omega)}. \end{aligned}$$

In light of (5), initial values are obtained from

$$u_i^{\alpha,0} = u_0 \cdot \left\langle \Phi_\alpha^{N_{\mathrm{r}}},\, \Phi_{0,0}^0 \right\rangle_{L^2(\Omega)} \quad \text{for } \alpha = 0, \dots, M-1.$$

4 Adaptivity in the stochastic space

In this section we exploit the possibilities to further reduce computational effort by applying adaptivity to the stochastic dimensions. We consider N_{r}-adaptivity, which was introduced in [9] for $N = 1$ and extend this method to several stochastic dimensions ($N \geq 2$). The concept of N_{r}-adaptivity requires a method for the computation of so-called "details". This means the quantification of the information that will get lost by the re-coarsening step $N_{\mathrm{r}} \to N_{\mathrm{r}} - 1$. We use the concept of a multi-wavelet basis for this purpose. For further reading we refer to [4, 12, 24, **?**, **?**].

4.1 Multi-wavelet basis

Similarly to Section 3.4.1 we start with the explanation by limiting ourselves to the case of a single stochastic dimension. Here $\theta = \theta(\omega)$ is again a random variable on the probability space $(\Omega, \mathcal{P}, \mathcal{F})$ that is assumed to satisfy $\theta \in L^2(\Omega)$ and $\theta \sim \mathcal{U}(0,1)$. For $N_{\mathrm{o}} \in \mathbb{N}_0$ and $N_{\mathrm{r}} \in \mathbb{N}_0$ the orthogonal basis of the space $S^{N_{\mathrm{o}},\, N_{\mathrm{r}}}$ defined in (13) is given by rescaled Legendre polynomials $\phi_{0,0}^{N_{\mathrm{r}}}, \dots, \phi_{N_{\mathrm{o}},2^{N_{\mathrm{r}}}-1}^{N_{\mathrm{r}}}$. The multi-wavelet subspace $W^{N_{\mathrm{o}},\, N_{\mathrm{r}}} \subset S^{N_{\mathrm{o}},\, N_{\mathrm{r}}+1}$ is defined as the orthogonal complement of $S^{N_{\mathrm{o}},\, N_{\mathrm{r}}}$, i.e.,

$$W^{N_{\mathrm{o}},\, N_{\mathrm{r}}} := (S^{N_{\mathrm{o}},\, N_{\mathrm{r}}})^\perp.$$

(For a comprehensive description of the construction of the orthonormal wavelet basis we refer to [2, 3, 29].) In what follows, we denote by $\{\psi_0, \dots, \psi_{N_{\mathrm{o}}}\}$ an orthonormal basis of $W^{N_{\mathrm{o}},\, 0}$. This means that

$$\langle \psi_i,\, \psi_j \rangle = \delta_{ij} \quad \text{for } 0 \leq i, j \leq N_{\mathrm{o}}.$$

The relation $S^{N_\mathrm{o},0} \perp W^{N_\mathrm{o},0}$ implies

$$\left\langle \psi_j,\, x^i \right\rangle = 0 \quad \text{for } 0 \le i,j \le N_\mathrm{o}.$$

The space $W^{N_\mathrm{o},N_\mathrm{r}}$ is spanned by multi-wavelets $\psi_{i,l}^{N_\mathrm{r}}$ given by

$$\psi_{i,l}^{N_\mathrm{r}}(\xi) = 2^{N_\mathrm{r}/2}\psi_i(2^{N_\mathrm{r}}\xi - l), \quad i = 0,\dots,N_\mathrm{o}, \quad l = 0,\dots,2^{N_\mathrm{r}}-1, \tag{21}$$

and their support is

$$\mathrm{supp}(\psi_{i,l}^{N_\mathrm{r}}) \subseteq I_l^{N_\mathrm{r}} := [2^{-N_\mathrm{r}}l, 2^{-N_\mathrm{r}}(l+1)].$$

4.2 Multivariate multi-wavelets

Similarly to the extension to the multivariate polynomial $\Phi_{\mathfrak{p},l}^{N_\mathrm{r}}$ in Section 3.4.2 we extend the definition of the multi-wavelet to their multivariate version. For this purpose we define the index vector

$$\boldsymbol{\alpha}_i := (p_i, l_i, \eta_i)^\mathrm{T} \in \boldsymbol{\mathcal{A}} := \{0,\dots,N_\mathrm{o}\} \times \{0,1\} \times \mathcal{I} \quad \text{for } i = 1,\dots,N,$$

and extend the definition of the multi-wavelet $\psi_{i,l}^{N_\mathrm{r}}$ (defined by (21)) to

$$\psi_{\boldsymbol{\alpha}_i}^{N_\mathrm{r}}(\xi) := \begin{cases} \psi_{p_i,l_i}^{N_\mathrm{r}}(\xi) & \text{if } \eta_i = 1, \\ \phi_{p_i,l_i}^{N_\mathrm{r}}(\xi) & \text{if } \eta_i = 0, \end{cases} \quad \boldsymbol{\alpha_i} \in \boldsymbol{\mathcal{A}}.$$

Here $l_i \in \tilde{\mathcal{I}}$ denotes the index of the stochastic element $I_{l_i}^{N_\mathrm{r}}$. Now we can define the multivariate multi-wavelet

$$\Psi_{\boldsymbol{\alpha}}^{N_\mathrm{r}}(\xi) := \prod_{i=1}^{N} \psi_{\boldsymbol{\alpha}_i}^{N_\mathrm{r}}(\xi_i), \quad \boldsymbol{\alpha} := (\boldsymbol{\alpha}_1,\dots,\boldsymbol{\alpha}_N) \in \boldsymbol{\mathcal{A}}^N.$$

The vector $l \in \mathcal{I}$ is the index of the corresponding stochastic element $I_{N,l}^{N_\mathrm{r}}$ given by (15). The multivariate multi-wavelets $\Psi_{\boldsymbol{\alpha}}^{N_\mathrm{r}}$ still remain orthonormal, namely

$$\left\langle \Psi_{\boldsymbol{\alpha}}^{N_\mathrm{r}}, \Psi_{\boldsymbol{\beta}}^{N_\mathrm{r}} \right\rangle = \delta_{\boldsymbol{\alpha},\boldsymbol{\beta}} \quad \text{for } \boldsymbol{\alpha},\boldsymbol{\beta} \in \boldsymbol{\mathcal{A}}^N.$$

Furthermore, for $\boldsymbol{\alpha} \in \boldsymbol{\mathcal{A}}^N$ we denote by $|\boldsymbol{\alpha}| := l \in \mathcal{I}$.

4.3 N_r-adaptivity

The algorithm of the adaptive multiresolution scheme for deterministic two-dimensional problems was introduced in [10–12] and extended to random perturbed problems with one random variable in [9]. Now we extend the method to the severally stochastic dimensions.

We first introduce the concept of a multi-dimensional graded tree for dealing with the HSG-FV data structure. As usual, a *node* is an element of the tree that represents a control volume of a mesh, defined by the stochastic element $I_{N,l}^m$ for $0 \le m \le L$ in (15). Here L denotes the level with the finest mesh. The *root* is the basis of the tree, represented by the stochastic element $I_{N,0}^0$. A node is called *leaf* when it has no children. Each parent node has 2^N children. Fig. 3 shows an example for the structure of the graded tree for $L = 3$, $N = 2$.

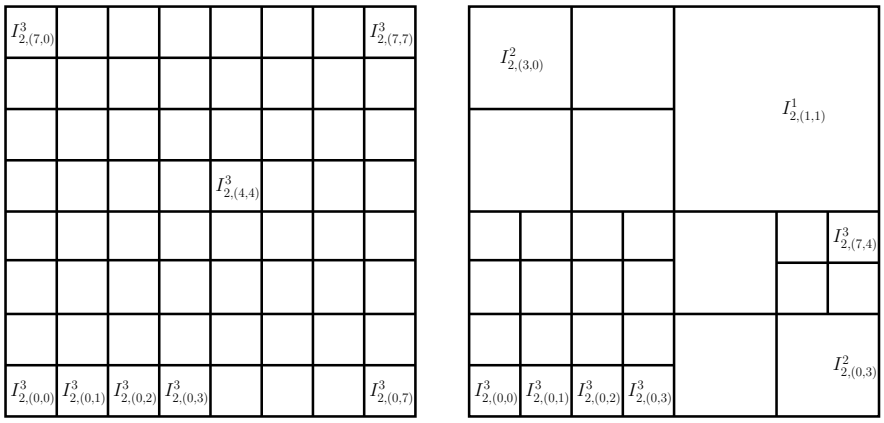

(a) Mesh for $N_\mathrm{r} = 3$, $N = 2$ (b) Resulting mesh

Fig. 3 Sketch of the adapted graded tree structure for $N = 2$, $L = 3$.

Let us proceed with the description of the re-meshing subroutine. In our notation, Λ denotes the set of the indices of the existing nodes, $\mathcal{L}(\Lambda)$ denotes the set of leaves and $N(\mathcal{L}(\Lambda))$ is the set of parents of the elements in $\mathcal{L}(\Lambda)$, and the set $\mathcal{L}(I^m_{N,k})$ denotes the set of leaves of the parent element $I^m_{N,k}$. The sets Λ^{del} and Λ^{ref} contain the indices of nodes that should be deleted respectively refined. A basic idea of our re-meshing strategy is to consider the difference of the data on the leaves and the projection of the data on their parent node in each time step and spatial point. For the computing of that difference called "details" we use the multivariate multi-wavelets introduced in Section. 4.2. The difference between a leaf $I^{m+1}_{N,l}$ and its parent node $I^m_{N,k}$ for the random field $w \equiv w(x,t,\theta(\boldsymbol{\omega})) \in L^2(\Omega)$ is represented by the "detail" coefficient $d^{m+1}_{k,l,r}$ in the direction $r = 1,\dots,N$ given by the following expression, where $\boldsymbol{e}_r$ denotes the r-th N-dimensional unit vector:

$$
\begin{aligned}
d^{m+1}_{k,l,r} &:= \sum_{\substack{|\alpha|=k,\\ (\eta_1,\dots,\eta_N)^{\mathrm{T}}=\boldsymbol{e}_r}} \left| \left\langle \sum_{|\mathfrak{p}|=0}^{N_\mathrm{o}} w^{l+1}_{\mathfrak{p},l} \Phi^{m+1}_{\mathfrak{p},l},\, \Psi^m_\alpha \right\rangle \right| \\
&= \sum_{\substack{|\alpha|=k,\\ (\eta_1,\dots,\eta_N)^{\mathrm{T}}=\boldsymbol{e}_r}} \left| \sum_{|\mathfrak{p}|=0}^{N_\mathrm{o}} w^{l+1}_{\mathfrak{p},l} \langle \Phi^{m+1}_{\mathfrak{p},l}, \Psi^m_\alpha \rangle \right|.
\end{aligned}
$$

We define the tolerance ε and the coarsest refinement level $C \geq 0$. In our computations C is given by the number of MPI ranks used.

Algorithm 1 explains our re-meshing procedure. Together with the re-meshing algorithm we can introduce an algorithm for the computation of the numerical solution (Algorithm 2). For the computation of the numerical flux between spatial elements with the different refinement level we use virtual nodes with the finer refinement level.

Algorithm 1 Re-meshing $(\Lambda, \varepsilon_{\mathrm{ref}}, \varepsilon_{\mathrm{coarse}})$

for $I_{N,k}^m \in N(\mathcal{L}(\Lambda))$ **do**
  for $I_{N,l}^{m+1} \in \mathcal{L}(I_{N,k}^m)$ **do**
    if $d_{k,l,q}^{m+1} > \varepsilon_{\mathrm{ref}}$ for one $q = 1, \dots, N$ **then**
      $\Lambda^{\mathrm{ref}} \leftarrow \Lambda^{\mathrm{ref}} \cup (l, m+1)$
    end if
    if $d_{k,l,q}^{m+1} < \varepsilon_{\mathrm{coarse}}$ for all $q = 1, \dots, N$ **then**
      $\Lambda^{\mathrm{del}} \leftarrow \Lambda^{\mathrm{del}} \cup (l, m+1)$
    end if
  end for
  if $\Lambda^{\mathrm{del}} \neq \emptyset$ **and** $\mathcal{L}(I_{N,k}^m) \not\subset \Lambda^{\mathrm{del}}$ **then**
    $\Lambda^{\mathrm{del}} \leftarrow \Lambda^{\mathrm{del}} \setminus (\Lambda^{\mathrm{del}} \cap \mathcal{L}(I_{N,k}^m))$
  end if
end for
for $(l, m) \in \Lambda^{\mathrm{del}}$ **do**
  if $m > C$ **then**
    $\Lambda \leftarrow \Lambda \setminus (l, m)$
  end if
end for
for $(l, m) \in \Lambda^{\mathrm{ref}}$ **do**
  $\Lambda \leftarrow \Lambda \cup (2^N l, m+1) \cup \cdots \cup (2^N l + 2^N - 1, m+1)$
end for
return Λ

Algorithm 2 Finite volume method with N_{r}-adaptivity

while $t < T$ **do**
  Calculate $\triangle t$.
  Compute $u(t + \triangle t)$ for all leaves in $\mathcal{L}(\Lambda)$.
  Re-meshing$(\Lambda, \varepsilon_{\mathrm{ref}}, \varepsilon_{\mathrm{coarse}})$ (Algorithm 1).
  $t \leftarrow t + \triangle t$
end while

5 Numerical experiments

5.1 Numerical experiments without stochastic adaptivity

We now illustrate the performance if the hybrid stochastic Galerkin finite volume (HSG-FV) method described in Section 3.4 and compare results with a reference solution generated by a Monte Carlo finite volume (MC-FV) scheme.

We start with the description of the scenarios considered for numerical experiments with two and three stochastic dimensions, then we proceed with the results of the numerical simulations and analyze the accuracy and efficiency of the method presented. The point of interest for the application is the determination of steady-state solutions of (5) with respect to the uncertainty represented by the random vector $\theta = (\theta_1, \theta_2, \theta_3)$. In particular, the random input is given by the randomly perturbed parameters $u_{\mathrm{F}}(\theta_1)$, $q_{\mathrm{L}}(\theta_2)$ and $q_{\mathrm{R}}(\theta_3)$ for random variables $\theta_1, \theta_2, \theta_3 \sim \mathcal{U}(0, 1)$. Thus, the unknown u depends on the random vector θ, and whether the solution indeed attains a steady state depends on the value of θ. For example, within the standard (deterministic) setting a steady state can be attained for the choice

$$u_{\mathrm{F}} = 0.15, \quad q_{\mathrm{L}} = -7.2 \cdot 10^{-6}\,\mathrm{m\,d^{-1}}, \quad q_{\mathrm{R}} = 3.0 \cdot 10^{-6}\,\mathrm{m\,s^{-1}}. \tag{22}$$

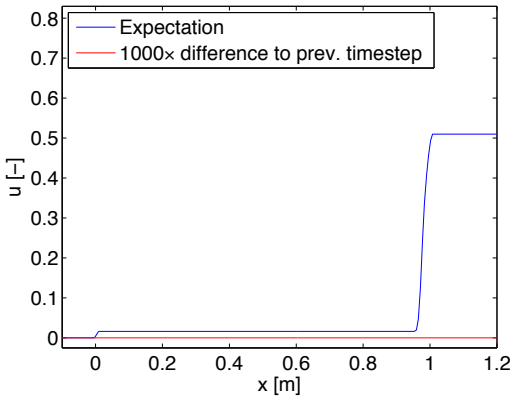

Fig. 4 Steady state for the parameter values u_{F}, q_{L} and q_{R} given by (22) at $T = 10^6$. Blue line: (deterministic) numerical solution, red line: difference to previous time step.

No.	N	u_{F}	q_{L} [m s^{-1}]	q_{R} [m s^{-1}]
1	1	$0.15 + 0.05\theta_1$	$-7.2 \cdot 10^{-6}$	$3.0 \cdot 10^{-6}$
2	1	0.15	$-7.2 \cdot 10^{-6} - 10^{-6}\theta_2$	$3.0 \cdot 10^{-6}$
3	1	0.15	$-7.2 \cdot 10^{-6}$	$3.0 \cdot 10^{-6} + 2.0 \cdot 10^{-6}\theta_3$
4	2	$0.15 + 0.05\theta_1$	$-7.2 \cdot 10^{-6} - 10^{-6}\theta_2$	$3.0 \cdot 10^{-6}$
5	2	$0.15 + 0.25\theta_1$	$-7.2 \cdot 10^{-6} - 5 \cdot 10^{-6}\theta_2$	$3.0 \cdot 10^{-6}$
6	3	$0.15 + 0.05\theta_1$	$-7.2 \cdot 10^{-6} - 10^{-6}\theta_2$	$3.0 \cdot 10^{-6} + 2.0 \cdot 10^{-6}\theta_3$
7	3	$0.15 + 0.25\theta_1$	$-7.2 \cdot 10^{-6} - 5 \cdot 10^{-6}\theta_2$	$3.0 \cdot 10^{-6} + 10^{-5}\theta_3$

Table 1 Scenarios with radom perturbations for $N = 1, 2, 3$.

Figure 4 shows the numerical solution (blue line) for this case at time $T = 10^6$ s. The plot of the difference to the previous time step (red line) shows that there is no difference to the previous timestep. In other words the solution shown is stationary. For the discussion of the appropriate conditions on γ^1, γ^2, u_{F} and b we refer to Section 2.

In the numerical examples we consider problem (5) with several random perturbations for $N = 1, 2, 3$, described by the scenarios listed in Table 1 and initial distribution $u_0 \equiv 0$. For the spatial discretization we use 400 mesh points for the x-interval $[-1.2, 1.2]$. We start with Scenario 4 that features two random perturbations (namely in u_{F} and q_{L}). The expectation and variance of the numerical solution are presented in Figure 5. This test case can be considered as a combination of two stochastically one-dimensional test cases, namely Scenarios 1 and 2. Their expectation and variance at $T = 2.5 \cdot 10^5$ s for $N_{\mathrm{r}} = 4$, $N_{\mathrm{o}} = 4$ are shown in Figures 5 (c) to (f). The reconstruction of the numerical solution for Scenarios 1 and 2 is shown in Figure 6.

To analyze the accuracy of the method we compare the expectation computed by the HSG-FV method with the Monte Carlo (MC) mean value, obtained by 10^6 samples. Figure 10(a) displays the comparison between the MC mean value computed with 10^6 samples and the expectation computed with HSG-FV method for Scenarios 4 (Figure 7(a)) and 5 (Figure 7(b)) and different choices of N_{r} and N_{o}. We observe that for Scenario 4 the HSG-FV results match the MC result exactly for most choices of N_{r} and N_{o}. Therefore to emphasize the influence of the random perturbation we use Scenario 5 for the analysis of convergence. Table 2 shows the L^1-error for $N_{\mathrm{r}} = 0, \ldots, 5$ and $N_{\mathrm{o}} = 0, \ldots, 3$. The presented

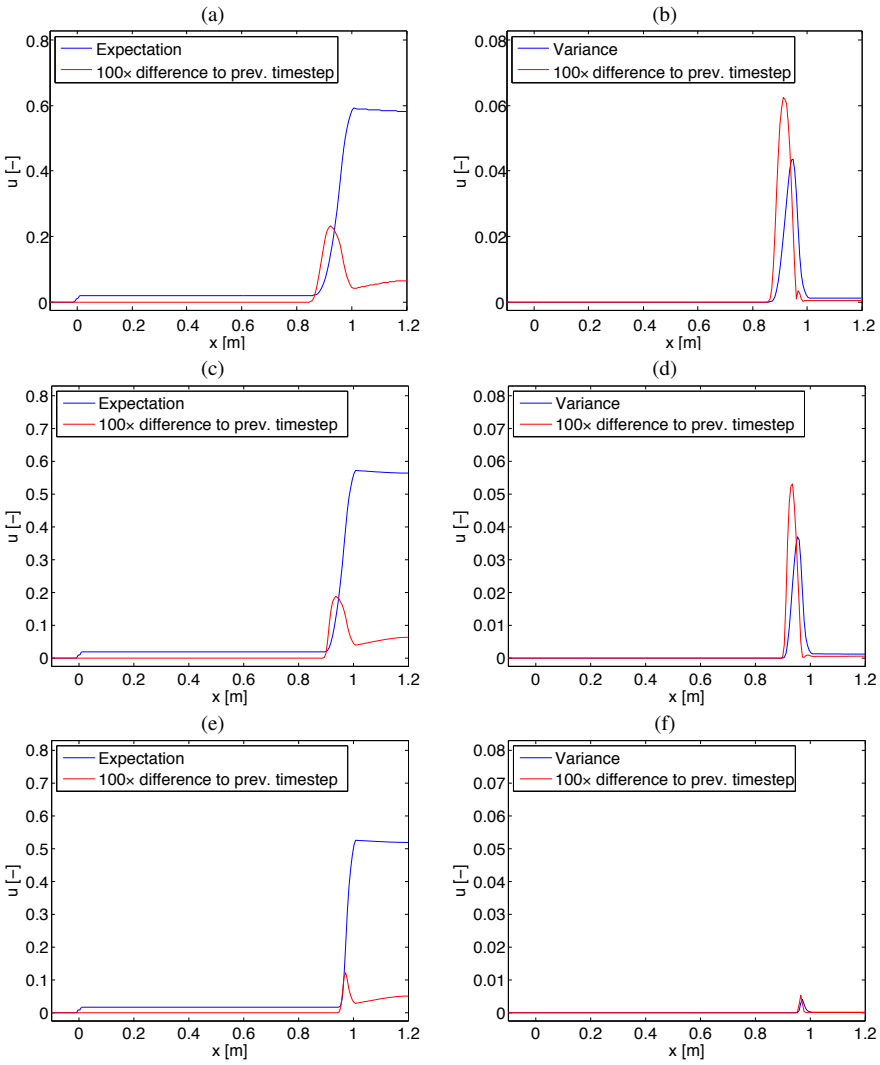

Fig. 5 Numerical solution at $T = 2.5 \cdot 10^5$ s computed with HSG-FV method (a, b) Scenario 4 for $N_\mathrm{r} = 4$, $N_\mathrm{o} = 3$, (c, d) Scenario 1 for $N_\mathrm{r} = 4$, $N_\mathrm{o} = 4$, (e, f) Scenario 2 for $N_\mathrm{r} = 4$, $N_\mathrm{o} = 4$, (a, c, e) expectation (blue line) and the difference to the previous time step (red line), (b, d, f) variance (blue line) and the difference to the previous time step (red line).

results clearly indicate the convergence of the HSG-FV expectation to the MC mean for increasing N_r and N_o.

In the next step we proceed with numerical examples for $N = 3$ random perturbations given by Scenario 6. Figure 8 shows again the expectation and variance of the numerical solution at $T = 2.5 \cdot 10^5$ s. The single components of Scenario 6 are given by Scenarios 1, 2 and 3. Their expectation, variance and reconstruction are shown in Figures 5 (c)–(f), 6 and 9.

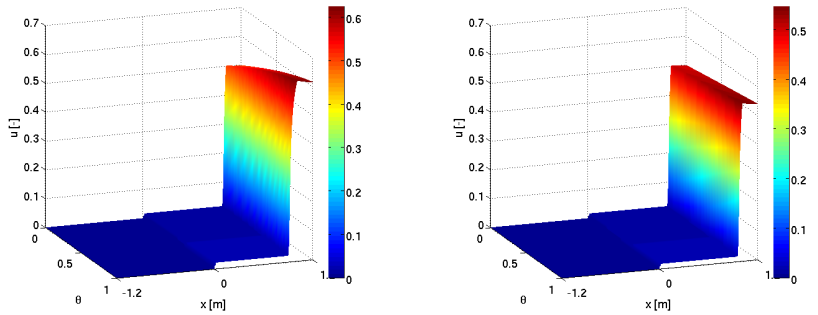

(a) (b)

Fig. 6 Reconstruction of the numerical solution (a) for Scenario 1; (b) for Scenario 2 at $T = 2.5 \cdot 10^5$ s computed with HSG-FV method for $N_\mathrm{r} = 4$, $N_\mathrm{o} = 4$.

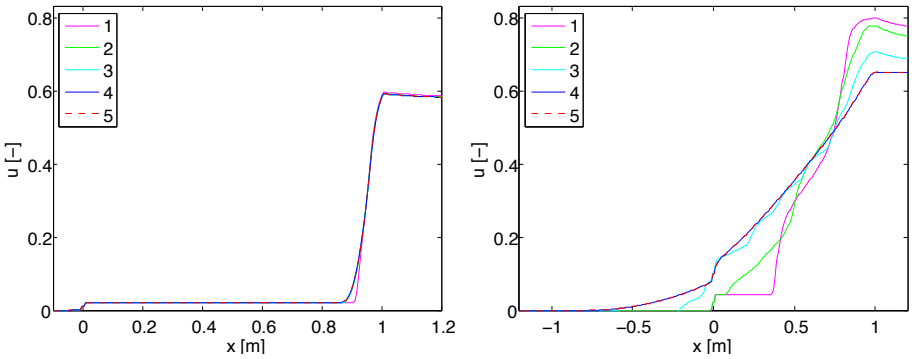

(a) (b)

Fig. 7 Expectation of the numerical solution (a) for Scenario 4; (b) for Scenario 5 at $T = 2.5 \cdot 10^5$ s computed with (1) $N_\mathrm{r} = 0$, $N_\mathrm{o} = 1$; (2) $N_\mathrm{r} = 0$, $N_\mathrm{o} = 3$; (3) $N_\mathrm{r} = 1$, $N_\mathrm{o} = 2$; (4) $N_\mathrm{r} = 5$, $N_\mathrm{o} = 3$; (5) 10^6 MC-samples.

The HSG-FV representation of the numerical solution allows a memory-efficient storage of simulation data. We only save the coefficients $u^0, \ldots, u^P$ for each mesh point and time step. But these data allow us to reconstruct the numerical solution for each value of $\theta \in [0,1]^3$. Par example Fig. 10 shows reconstructions for Scenarios 4 and 6 for several choices of $\theta \in [0,1]^N$, $N = 2, 3$.

The simulations are performed on a computer cluster built up by $2\times$ Intel(R) Xeon(R) CPU E5-2680 v2 (2.80GHz, 10 Cores) per node, by using MPI+OpenMP parallelisation for $N_\mathrm{r} > 0$, $N_\mathrm{o} > 0$ and OpenMP, MPI only for $N_\mathrm{r} = 0$, $N_\mathrm{o} = 0$. The further reduction of the computation time of the HSG-FV method by the parallelisation and adaptivity that is introduced in Section 4. Numerical examples illustrating these improvements are discussed in Section 5.2.

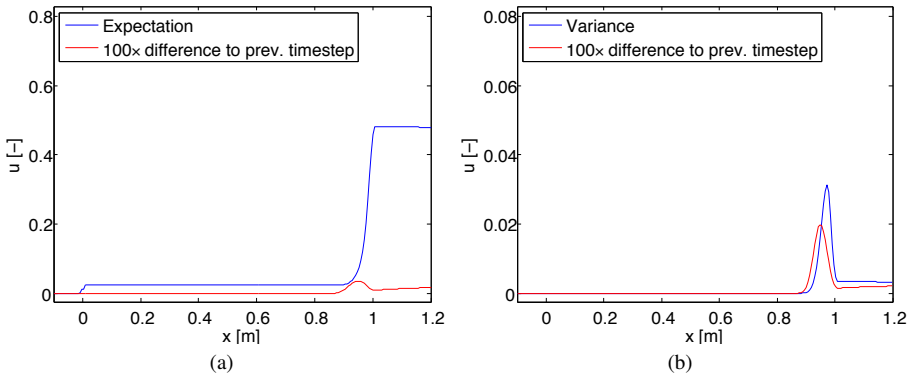

(a) (b)

Fig. 8 Numerical solution for Scenario 6 at $T = 2.5 \cdot 10^5$ s computed with HSG-FV method for $N_\mathrm{r} = 2$, $N_\mathrm{o} = 2$. (a) Expectation (blue line) and the difference to the previous time step (red line). (b) Variance (blue line) and the difference to the previous time step (red line).

Table 2 L^1-error for Scenario 5, at $T = 2.5 \cdot 10^5$ s. Compared with Monte Carlo result over 10^6 samples.

N_o	$N_\mathrm{r} = 0$	$N_\mathrm{r} = 1$	$N_\mathrm{r} = 2$	$N_\mathrm{r} = 3$	$N_\mathrm{r} = 4$	$N_\mathrm{r} = 5$
0	1.76e-01	4.37e-02	1.22e-02	2.74e-03	7.89e-04	5.56e-04
1	1.69e-01	5.94e-02	2.12e-02	4.40e-03	2.12e-03	1.30e-03
2	1.58e-01	4.89e-02	1.45e-02	4.53e-03	2.39e-03	1.24e-03
3	1.29e-01	3.50e-02	1.06e-02	4.85e-03	2.21e-03	1.01e-03

Table 3 L^1-error for Scenario 7, at $T = 2.5 \cdot 10^5$ s. Compared with Monte Carlo result over 10^6 samples.

N_o	$N_\mathrm{r} = 0$	$N_\mathrm{r} = 1$	$N_\mathrm{r} = 2$	$N_\mathrm{r} = 3$
0	1.05e-01	2.67e-02	6.32e-03	1.59e-03
1	9.15e-02	3.34e-02	1.28e-02	4.83e-03
2	6.25e-02	4.04e-02	1.47e-02	5.41e-03

5.2 Efficiency and parallel application

The application of the HSG-FV approach yields a high-dimensional system. The structure of this system allows the parallel computation of the coefficients $u^0, \ldots, u^P$ in each time step. We now provide a brief overview of the implementation of the HSG-FV approach from a parallelization point of view, and discuss the computational efficiency of the hybrid parallelisation of the HSG-FV approach by MPI+OpenMP.

The dimension of the system resulted from the HSG discretisation for a given stochastic dimension N depends on the two parameters N_r and N_o. The first parameter N_r determines the number of the stochastic elements (SE) $I_{N,l}^{N_\mathrm{r}}$, where $l = 0, \ldots, 2^{NN_\mathrm{r}} - 1$. The decoupled structure of the stochastic elements allows an efficient parallelization on the distributed memory architectures e.g. MPI, by restriction of each computation node to one or several certain stochastic elements. This restriction allows to reduce or omit the communication between the computation nodes, because the computations on each stochastic element could be performed independently from the other stochastic elements. The polynomial order N_o determines the size of the system on each stochastic element $I_{N,l}^{N_\mathrm{r}}$, given

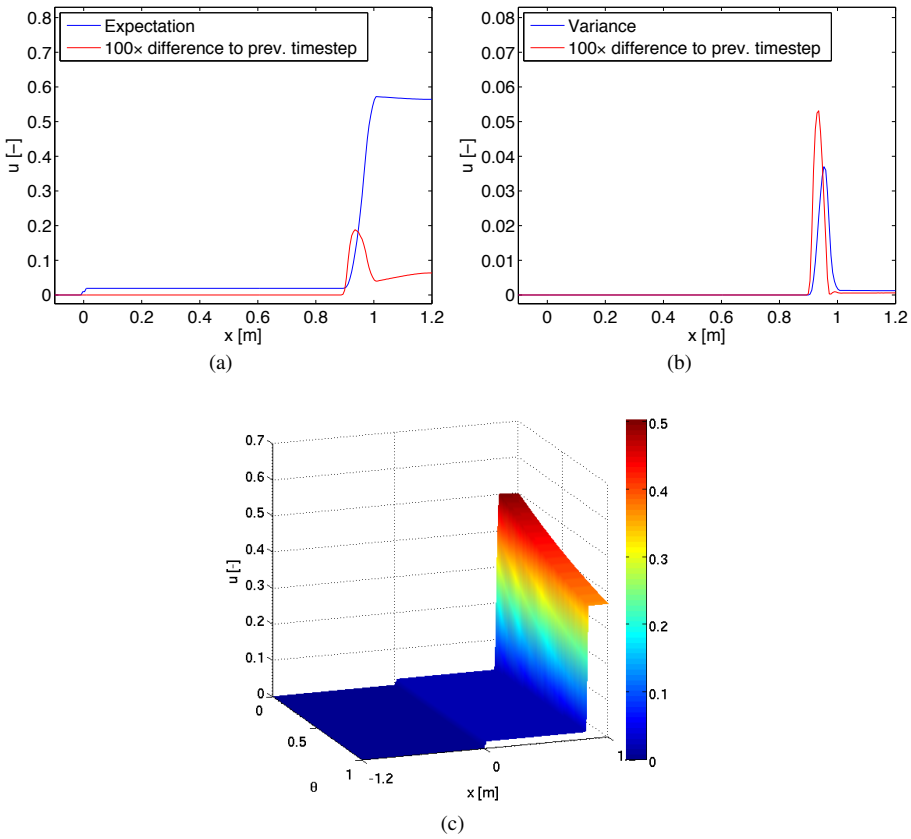

Fig. 9 Numerical solution for Scenario 3 at $T = 2.5 \cdot 10^5$ s computed with the HSG-FV method for $N_\mathrm{r} = 2$, $N_\mathrm{o} = 1$. (a) Expectation (blue line) and the difference to the previous time step (red line). (b) Variance (blue line) and the difference to the previous time step (red line). (c) Reconstruction of the numerical solution.

by $(N_\mathrm{o} + N)!/[N_\mathrm{o}!N!]$. Computations of entries of the Jacobian and fluxes in each dimension can be also performed in parallel, but since the system is not decoupled the coefficients $u^0, \ldots, u^P$ should be synchronised in each time step. This implies that the efficient parallelisation requires fast communication. In particular, this can be achieved by using shared memory machines and OpenMP. For these reasons we use the hybrid parallelisation with MPI parallelisation over stochastic elements and OpenMP parallelisation over the polynomial order.

As a first example, consider the computations for $N = 2$ and Scenario 5. The computational times are presented in Table 4. The computations are performed on one node 2×Intel(R) Xeon(R) CPU E5-2680 v2 (2.80GHz) (10 cores with hyper-threading). For $N_\mathrm{r} = 0$ we use one MPI rank with up to 10 OpenMP threads, for $N_\mathrm{r} = 1$ we use 4 MPI ranks each with up to 5 OpenMP threads and for $N_\mathrm{r} \geq 2$ we use 16 MPI ranks each with up to 2 OpenMP threads.

Let us proceed with Scenario 7 for $N = 3$. Tab. 5 shows the computational times for $N_\mathrm{r} = 0, \ldots, 3$ and $N_\mathrm{o} = 0, \ldots, 2$ on 1-4 nodes. For $N_\mathrm{r} = 0$ we use one MPI rank and up

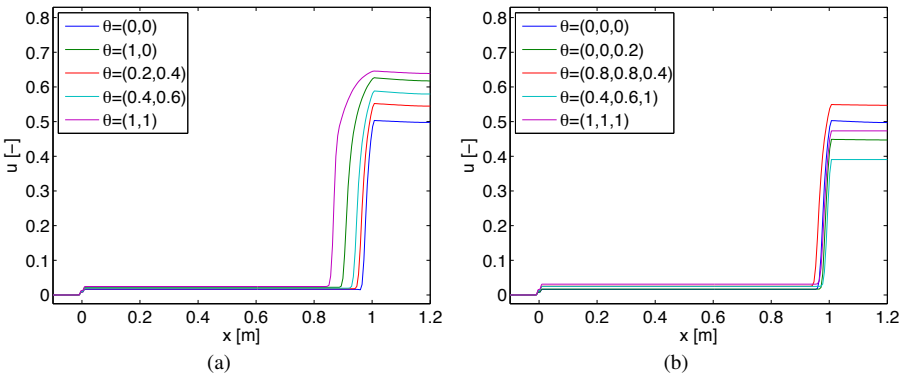

Fig. 10 Reconstructions of the numerical solutions at $T = 2.5{\cdot}10^5$ s computed with the HSG-FV method for $N_\mathrm{r} = 3$, $N_\mathrm{o} = 1$. (a) Reconstructions for the scenario 4 for several values of $\theta \in [0,1]^2$. (b) Reconstructions for the scenario 6 for several values of $\theta \in [0,1]^3$.

Table 4 Duration (in seconds) of HSG-FV computation on Intel(R) Xeon(R) CPU E5-2680 v2 (2.80GHz), using one node (20 cores with hyper-threading), for Scenario 5 at $T = 2.5 \cdot 10^5$ s.

N_r/ #SE	0 / 1	1 / 4	2 / 16	3 / 64	4 / 256	5 / 1024
N_o=0	108	113	114	489	1976	8143
N_o=1	523	387	6168	2672	10537	42243
N_o=2	1472	1085	2913	12415	47468	202641
N_o=3	3209	3208	9369	38150	147541	616596

Table 5 Duration (in seconds) of HSG-FV computation on Intel(R) Xeon(R) CPU E5-2680 v2 (2.80GHz), using 1-4 nodes (20 cores with hyper-threading) for Scenario 7 at $T = 2.5 \cdot 10^5$ s.

N_r/ #SE	0 / 1	1 / 8	2 / 64	3 / 512
N_o=0	1322	1497	11254	13657
N_o=1	8204	8470	67480	113220
N_o=2	33670	45531	348102	714583

Table 6 Duration (in seconds) of HSG-FV computation on 1-16 nodes (2×Intel(R) Xeon(R) CPU E5-2680 v2 (2.80GHz)) for Scenario 5 with $N_\mathrm{r} = 4$, at $T = 2.5 \cdot 10^5$ s.

#Nodes / #CPU	1 / 20	2 / 40	4 / 80	8 / 160	16 /320
N_o=2	57073	28853	14329	7558	3536
N_o=3	180930	91874	45262	23217	10736

to 5 OpenMP threads, for $N_\mathrm{r} = 1, 2$ we use 8 MPI ranks each with up to 5 OpenMP threads on one computing node, for $N_\mathrm{r} = 3$ we use 64 MPI ranks each with up to 2 OpenMP threads on 4 computing nodes.

In the next step let us discuss the strong scaling of the parallel execution of the method. For this purpose let us again consider Scenario 5 with $N_\mathrm{r} = 4$, $N_\mathrm{o} = 2, 3$. Table 6 shows the computational times on 20-320 CPU cores.

The computational times presented show that the strong scaling of the method is almost linear for an appropriate number of cores. We can see that hybrid parallelisation allows us

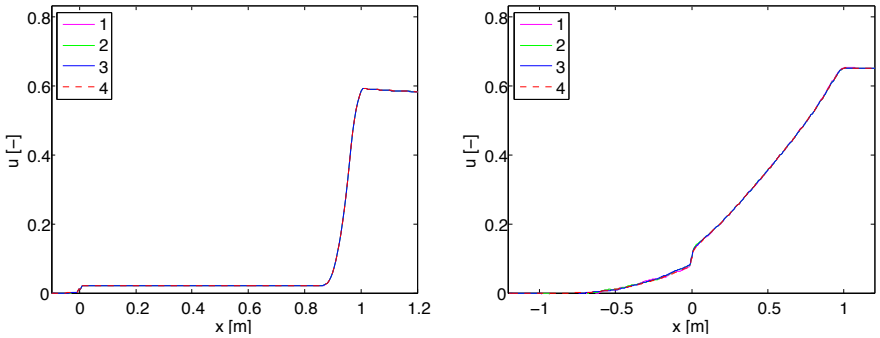

Fig. 11 Expectation of the numerical solution with N_r-adaptivity (a) for Scenario 4; (b) for Scenario 5 at $T = 2.5 \cdot 10^5$ s computed with (1) $N_\mathrm{r} = 3$, $N_\mathrm{o} = 1$; (2) $N_\mathrm{r} = 4$, $N_\mathrm{o} = 1$; (3) $N_\mathrm{r} = 5$, $N_\mathrm{o} = 3$; (4) 10^6 MC-samples.

to perform efficient computations on single nodes and distributed systems. In particular, the MPI parallelisation over stochastic elements allows the use of several nodes without necessary of the fast communication between MPI ranks. Since the parallelisation over the polynomial order requires the complete synchronisation in each time step, the synchronisation effort increases significantly with the increasing number of threads. Therefore it is most promising to use the maximal possible number of MPI ranks together with a low number of the OpenMP threads.

5.3 Numerical experiments including stochastic adaptivity

Now we apply the stochastic adaptivity method presented in Section 4 to several examples for $N = 2, 3$.

We start with two numerical scenarios for $N = 2$: The scenario with low random perturbation given by Scenario 4, and the scenario with higher random perturbation is given by Scenario 5. For the presented computations we use one node build by $2\times$ Intel(R) Xeon(R) CPU E5-2680 v2 (2.80GHz). We use 16 MPI ranks each up to two OpenMP threads on 20 CPU cores.

Figure 11 shows the plots of the expectations of the N_r-adaptive HSG solutions for Scenarios 4 and 5 compared with appropriate MC solutions for 10^6 samples. We then consider the accuracy and computing time. Tables 7 and 8 show the L^1-error and computing times for the scenario with low random perturbation given by Scenario 4. Then we increase the random perturbation and consider Scenario 5. Tables 9 and 10 show the L^1-error and computing times for this test case. In both cases the HSG-FV method with and without N_r-adaptivity provides a similar accuracy. In case with lower random perturbation computations with N_r-adaptivity are up to four times faster then without. For stronger random perturbation the computations with N_r-adaptivity are up to two times faster.

Now let us discuss the application of the N_r-adaptivity for $N = 3$. For this purpose we use Scenario 6. Tab. 11 and 12 shows the L^1-error and computing times of the computations with and without N_r-adaptivity. Fig. 12 shows the plots of the expectations of the N_r-adaptive HSG solutions for Scenarios 6 and 7 compared with appropriate MC solutions

Table 7 L^1-error for Scenario 4 computed (a) without N_r-adaptivity; (b) with N_r-adaptivity threshold parameter 0.001 at $T = 2.5 \cdot 10^5$ s. Compared with Monte Carlo result over 10^6 samples.

(a)

N_o	$N_\mathrm{r} = 3$	$N_\mathrm{r} = 4$	$N_\mathrm{r} = 5$
0	7.56e-05	7.28e-05	3.93e-05
1	7.11e-05	8.23e-05	4.25e-05
2	7.92e-05	8.70e-05	4.44e-05
3	8.44e-05	8.96e-05	4.56e-05

(b)

N_o	$N_\mathrm{r} = 3$	$N_\mathrm{r} = 4$	$N_\mathrm{r} = 5$
0	8.36e-05	7.65e-05	7.65e-05
1	7.06e-05	6.90e-05	6.89e-05
2	7.87e-05	7.86e-05	7.86e-05
3	8.39e-05	1.08e-04	8.71e-05

Table 8 Duration (in seconds) of HSG-FV computation on Intel(R) Xeon(R) CPU E5-2680 v2 (2.80GHz), using 1 node (20 cores with hyper-threading), for Scenario 4, at $T = 2.5 \cdot 10^5$ s. (a) Without N_r-adaptivity; (b) with N_r-adaptivity (cf. Sect. 4).

(a)

N_o	N_r=3	N_r=4	N_r=5
0	492	2040	8138
1	2672	9547	41833
2	12415	48588	203340
3	39354	149530	624270

(b)

N_o	N_r=3	N_r=4	N_r=5
0	320	1049	1965
1	1657	5738	9184
2	7823	25079	37391
3	23510	81283	308670

Table 9 L^1-error for Scenario 5 computed (a) without N_r-adaptivity; (b) with N_r-adaptivity threshold parameter 0.001 at $T = 2.5 \cdot 10^5$. Compared with Monte Carlo result over 10^6 samples.

(a)

N_o	$N_\mathrm{r} = 3$	$N_\mathrm{r} = 4$	$N_\mathrm{r} = 5$
0	2.74e-03	7.89e-04	5.56e-04
1	4.40e-03	2.12e-03	1.30e-03
2	4.53e-03	2.39e-03	1.24e-03
3	4.85e-03	2.21e-03	1.01e-03

(b)

N_o	$N_\mathrm{r} = 3$	$N_\mathrm{r} = 4$	$N_\mathrm{r} = 5$
0	4.41e-03	4.35e-03	4.36e-03
1	3.98e-03	3.33e-03	3.29e-03
2	3.92e-03	3.34e-03	3.28e-03
3	4.46e-03	3.33e-03	3.09e-03

Table 10 Duration (in seconds) of HSG-FV computation on Intel(R) Xeon(R) CPU E5-2680 v2 (2.80GHz), using 1 Node (20 cores with hyper-threading), for Scenario 5, at $T = 2.5 \cdot 10^5$. (a) Without N_r-adaptivity; (b) with N_r-adaptivity (cf. Sect. 4).

(a)

N_o	N_r=3	N_r=4	N_r=5
0	489	1976	8143
1	2622	10537	42243
2	11747	47468	202641
3	38150	147541	616596

(b)

N_o	N_r=3	N_r=4	N_r=5
0	315	1054	4234
1	1655	5572	20633
2	7703	25613	91859
3	24454	82154	307937

for 10^6 samples. Similar to numerical experiments for $N = 2$ the N_r-adaptivity provides up to two times faster computations with the comparable accuracy.

Table 11 L^1-error for the test case Scenario 6 computed (a) without adaptivity; (b) with N_r-adaptivity threshold parameter 0.001 at $T = 2.5 \cdot 10^5$ s. Compared with Monte Carlo result over 10^6 samples.

(a)

N_o	$N_\mathrm{r} = 2$	$N_\mathrm{r} = 3$
0	3.01e-04	7.39e-05
1	1.68e-04	5.60e-05
2	1.12e-04	5.36e-05

(b)

N_o	$N_\mathrm{r} = 2$	$N_\mathrm{r} = 3$
0	2.45e-04	2.71e-04
1	1.67e-04	5.54e-05
2	1.12e-04	5.10e-05

Table 12 Duration (in seconds) of HSG-FV computation on Intel(R) Xeon(R) CPU E5-2680 v2 (2.80GHz), using 1-4 Node (20 cores with hyper-threading), for Scenario 6, at $T = 2.5 \cdot 10^5$. (a) Without N_r-adaptivity; (b) with N_r-adaptivity (cf. Sect. 4).

(a)

N_o	N_r=2	N_r=3
0	11480	12739
1	66258	116352
2	353577	699396

(b)

N_o	N_r=2	N_r=3
0	6546	5901
1	39894	62229
2	193146	377307

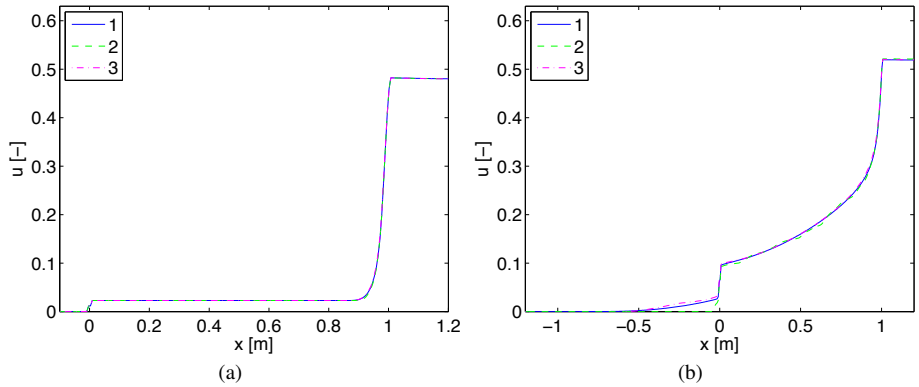

Fig. 12 Expectation of the numerical solution with N_r-adaptivity (a) for Scenario 6; (b) for Scenario 7 at $T = 2.5 \cdot 10^5$ s computed with (1) 10^6 MC-samples; (2) $N_\mathrm{r} = 2$, $N_\mathrm{o} = 0$; (3) $N_\mathrm{r} = 3$, $N_\mathrm{o} = 2$.

6 Application on the real-world problem

In this section we consider the application of the HSG-FV method on a realistic setting. Our point of interest in this section is the influence of the random perturbed parameters on the steady state solution. Therefore we start with a following deterministic scenario

$$u_\mathrm{F} = 0.35, \quad q_\mathrm{L} = -7.2 \cdot 10^{-6}\ \mathrm{m\,s^{-1}}, \quad q_\mathrm{R} = 1.25 \cdot 10^{-5}\ \mathrm{m\,s^{-1}}, \tag{23}$$

that yields the steady-state solution presented in Figure 13.

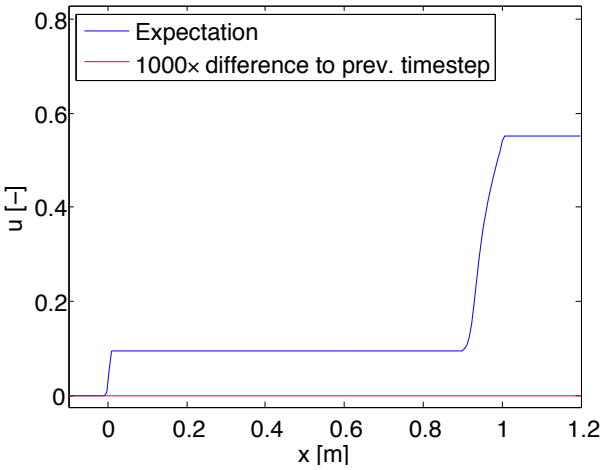

Fig. 13 Steady-state numerical solution at $T = 10^6$ for the scenario given in (23).

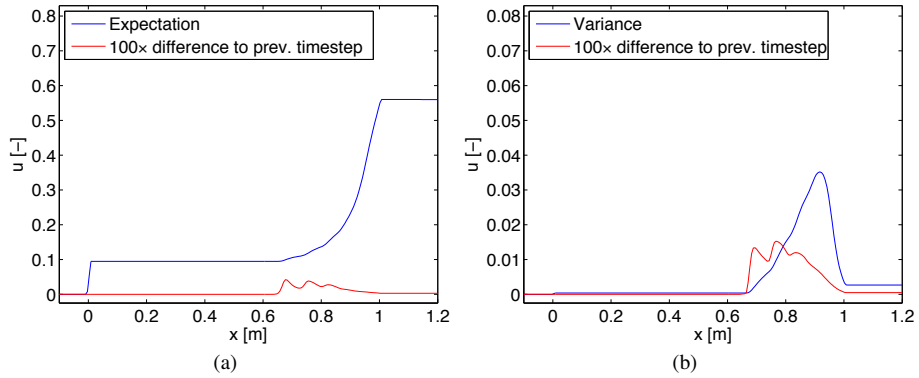

Fig. 14 Expectation (a) and variance (b) of the numerical solution for Scenario given in (24) at $T = 2.5 \cdot 10^5$ s computed with $N_\mathrm{r} = 2$, $N_\mathrm{o} = 1$.

In the next step we extend this scenario by three random parameters $\theta_1, \theta_2, \theta_3 \in \mathcal{U}(0,1)$ and obtain the following setting that provides three random perturbations of the setting (23)

$$u_F = 0.35 + 0.05(\theta_1 - 0.5), \quad q_\mathrm{L} = -7.2 \cdot 10^{-6} - (\theta_2 - 0.5) \cdot 10^{-6}\ \mathrm{m\,s^{-1}},$$
$$q_\mathrm{R} = 1.25 \cdot 10^{-5} + (\theta_3 - 0.5) \cdot 10^{-5}\ \mathrm{m\,s^{-1}}. \quad (24)$$

Now we can apply the HSG-FV method on the presented random disturbed setting, where the initial value in the numerical experiment below is given by the steady state solution of the Scenario (23) shown in Figure 13. A further advantage of the HSG method, is the possibility to compute a reconstruction of the numerical solution for each choice of $\theta \in [0,1]^3$ during the post-processing. The results of the numerical experiments are presented in Figures 14 and 15, where Figure 14 shows the expectation and variance at $T = 2.5 \cdot 10^5$ s and Figure 15 shows the reconstruction of the numerical solution for several choices of $\theta \in [0,1]^3$ at $T =$

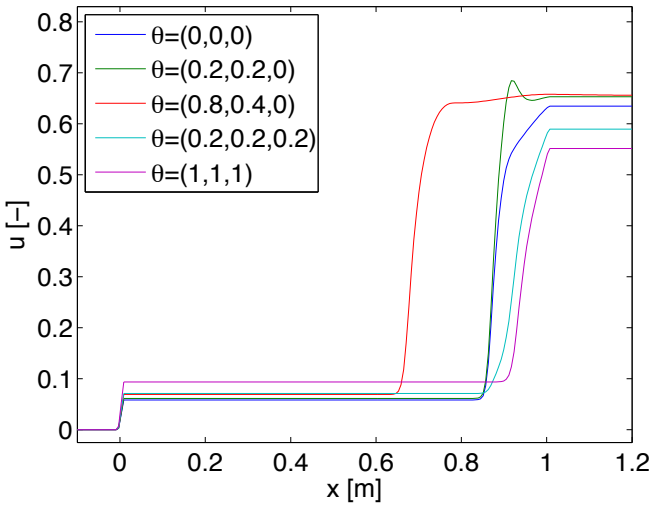

Fig. 15 Reconstruction of the numerical solution for Scenario (24) and several choices of $\theta \in [0,1]^3$ at $T = 2.5 \cdot 10^5$ s with initial value given by steady state solution in Fig. 13.

$2.5 \cdot 10^5$ s. We can see that the random-perturbed Scenario (24) yields a solution with non-stationary expectation and variance. In practical terms this means that if some of the control parameters are subject to stochastic variability expressed, for instance, by the parameters $(\theta_1, \theta_2, \theta_3) = (0.8, 0.4, 0)$, then one should expect that instead of attaining a state, the sediment in the thickening zone will start to rise, solid material enters the clarification zone, and the unit may overflow. It is precisely the purpose of the present approach to provide a tool that helps quantifying efficiently, and based on the uncertainty of the control or other parameters, whether this or other events are likely to occur.

7 Conclusions

In this paper, we discuss the application of the HSG-FV method on a clarifier-thickener problem with up to three random sources. Our numerical examples show, that the method allows us to obtain a fast and accurate approach. Further, the structure of the proposed stochastic discretisation allows efficient hybrid (MPI+OpenMP) parallelisation, that plays an important role for the computing on state-of-the-art cluster hardware. We complete our work with an stochastic adaptivity method, that allows us to reduce the computational effort, and in the same time still allows efficient parallel computation.

While the adaptive parallel HSG methods gives good numerical results for the CT operator it must be pointed out that the overall approach can be applied to a wide range of conservation laws with uncertain coefficients.

References

1. R. Abgrall. A simple, flexible and generic deterministic approach to uncertainty quantifications in non linear problems: application to fluid flow problems. Submitted to J. Comput. Phys., 2007.

2. B. K. Alpert. Wavelets and other bases for fast numerical linear algebra. In *Wavelets*, volume 2 of *Wavelet Anal. Appl.*, pages 181–216. Academic Press, Boston, MA, 1992.
3. B. K. Alpert. A class of bases in L^2 for the sparse representation of integral operators. *SIAM J. Math. Anal.*, 24(1):246–262, 1993.
4. B. L. Bihari and A. Harten. Application of generalized wavelets: an adaptive multiresolution scheme. *J. Comput. Appl. Math.*, 61(3):275–321, 1995.
5. R. Bürger, K. H. Karlsen, N. H. Risebro, and J. D. Towers. Well-posedness in BV_t and convergence of a difference scheme for continuous sedimentation in ideal clarifier-thickener units. *Numer. Math.*, 97(1):25–65, 2004.
6. R. Bürger, K. H. Karlsen, H. Torres, and J. D. Towers. Second-order schemes for conservation laws with discontinuous flux modelling clarifier-thickener units. *Numer. Math.*, 116:579–617, 2010.
7. R. Bürger, K. H. Karlsen, and J. D. Towers. A model of continuous sedimentation of flocculated suspensions in clarifier-thickener units. *SIAM J. Appl. Math.*, 65(3):882–940, 2005.
8. R. Bürger, K. H. Karlsen, and J. D. Towers. An Engquist-Osher-type scheme for conservation laws with discontinuous flux adapted to flux connections. *SIAM J. Numer. Anal.*, 47:1684–1712, 2009.
9. R. Bürger, I. Kröker, and C. Rohde. A hybrid stochastic Galerkin method for uncertainty quantification applied to a conservation law modelling a clarifier-thickener unit. *ZAMM Z. Angew. Math. Mech.*, 94(10):793–817, 2014.
10. R. Bürger, R. Ruiz, K. Schneider, and M. Sepúlveda. Fully adaptive multiresolution schemes for strongly degenerate parabolic equations in one space dimension. *M2AN Math. Model. Numer. Anal.*, 42(4):535–563, 2008.
11. R. Bürger, R. Ruiz-Baier, and K. Schneider. Adaptive multiresolution methods for the simulation of waves in excitable media. *J. Sci. Comput.*, 43(2):261–290, 2010.
12. R. Bürger, R. Ruiz-Baier, K. Schneider, and H. Torres. A multiresolution method for the simulation of sedimentation in inclined channels. *Int. J. Numer. Anal. Model.*, 9:479–504, 2012.
13. Raimund Bürger, Ilja Kröker, and Christian Rohde. Uncertainty quantification for a clarifier-thickener model with random feed. In *Finite volumes for complex applications. VI. Problems & perspectives. Volume 1, 2*, volume 4, pages 195–203. Springer, 2011.
14. R. H. Cameron and W. T. Martin. The orthogonal development of non-linear functionals in series of Fourier-Hermite functionals. *Ann. of Math. (2)*, 48:385–392, 1947.
15. J.-P. Chancelier, M. Cohen de Lara, and F. Pacard. Analysis of a conservation PDE with discontinuous flux: a model of settler. *SIAM J. Appl. Math.*, 54:954–995, 1994.
16. S. Diehl. A conservation law with point source and discontinuous flux function modelling continuous sedimentation. *SIAM J. Appl. Math.*, 56(2):388–419, 1996.
17. S. Diehl. Scalar conservation laws with discontinuous flux function: I. The viscous profile condition. *Comm. Math. Phys.*, 176:23–44, 1996.
18. S. Diehl. Operating charts for continuous sedimentation. I. Control of steady states. *J. Engrg. Math.*, 41(2-3):117–144, 2001. Sedimentation and suspension flows: some recent contributions (Stuttgart, 1999).
19. S. Diehl. Operating charts for continuous sedimentation. II. Step responses. *J. Engrg. Math.*, 53(2):139–185, 2005.
20. S. Diehl. Operating charts for continuous sedimentation. III. Control of step inputs. *J. Engrg. Math.*, 54(3):225–259, 2006.
21. S. Diehl. Operating charts for continuous sedimentation. IV. Limitations for control of dynamic behaviour. *J. Engrg. Math.*, 60(3-4):249–264, 2008.
22. B. Engquist and S. Osher. One-sided difference approximations for nonlinear conservation laws. *Math. Comp.*, 36:321–351, 1981.
23. R. G. Ghanem and P. D. Spanos. *Stochastic finite elements: a spectral approach*. Springer-Verlag, New York, 1991.
24. A. Harten. Multiresolution algorithms for the numerical solution of hyperbolic conservation laws. *Comm. Pure Appl. Math.*, 48(12):1305–1342, 1995.
25. M. Köppel, I. Kröker, and C. Rohde. Stochastic modeling for heterogeneous two-phase flow. In Jürgen Fuhrmann, Mario Ohlberger, and Christian Rohde, editors, *Finite Volumes for Complex Applications VII-Methods and Theoretical Aspects*, volume 77 of *Springer Proceedings in Mathematics & Statistics*, pages 353–361. Springer International Publishing, 2014.
26. Ilja Kröker, Wolfgang Nowak, and Christian Rohde. A stochastically and spatially adaptive parallel scheme for uncertain and nonlinear two-phase flow problems. *Computational Geosciences*, 19(2):269–284, 2015.
27. S. N. Kružkov. First order quasilinear equations with several independent variables. *Mat. Sb. (N.S.)*, 81 (123):228–255, 1970.
28. G. J. Kynch. A theory of sedimentation. *Trans. Faraday Soc.*, 48:166–176, 1952.

29. O. P. Le Maître, H. N. Najm, R. G. Ghanem, and O. M. Knio. Multi-resolution analysis of Wiener-type uncertainty propagation schemes. *J. Comput. Phys.*, 197(2):502–531, 2004.
30. H. G. Matthies and A. Keese. Galerkin methods for linear and nonlinear elliptic stochastic partial differential equations. *Comput. Methods Appl. Mech. Engrg.*, 194(12-16):1295–1331, 2005.
31. K. Oldham, J. Myland, and J. Spanier. *An atlas of functions*. Springer, New York, second edition, 2009.
32. G. Poëtte, B. Després, and D. Lucor. Uncertainty quantification for systems of conservation laws. *J. Comput. Phys.*, 228(7):2443–2467, 2009.
33. J. F. Richardson and W. N. Zaki. Sedimentation and fluidization: Part i. *Trans. Instn. Chem. Engrs. (London)*, 32:35–53, 1954.
34. J. Tryoen, O. Le Maître, M. Ndjinga, and A. Ern. Intrusive Galerkin methods with upwinding for uncertain nonlinear hyperbolic systems. *J. Comput. Phys.*, 229(18):6485–6511, 2010.
35. J. Tryoen, O. Le Maître, and A. Ern. Adaptive Anisotropic Spectral Stochastic Methods for Uncertain Scalar Conservation Laws. *SIAM J. Sci. Comput.*, 34(5):A2459–A2481, 2012.
36. A. Tveito and R. Winther. The solution of nonstrictly hyperbolic conservation laws may be hard to compute. *SIAM J. Sci. Comput.*, 16(2):320–329, 1995.
37. D. Xiu and G. E. Karniadakis. Modeling uncertainty in flow simulations via generalized polynomial chaos. *J. of Comput. Phys.*, 187(1):137–167, 2003.